Proposal for an experiment at PSI

Measurement of the strong interaction width and shift of the ground state of pionic hydrogen

G.C. Oades
Institute of Physics, Aarhus University, DK-8000 Aarhus, Denmark
S. Biri
Inst. of Nuclear Research (ATOMKI) of the Hungarian Academy of Sciences, H-4001, Debrecen
D. F. Anagnostopoulos
University of Ioannina, Greece
G. Borchert, D. Gotta
Institut für Kernphysik, Forschungsanlage Jülich, D-52425 Jülich, Germany
N. Nelms
Space Research Center, Department of Physics and Astronomy,University of Leicester, University Road, Leicester LE1 7RH, Great Britain
J.-P. Egger
Institut de Physique, Université de Neuchatel, Rue A.-L. Breguet CH-2000 Neuchatel
E. Bovet, G. Fiorucci
EISI, Rue Baptiste-Savoye 26 , CH-2610 St. Imier
P. Indelicato
Laboratoire Kastler–Brossel, Université Pierre et Marie Curie , 4 place Jussieu, F–75252 Paris Cedex 05, France
P. Hauser, P. A. Schmelzbach, L.M. Simons, V. E. Markushin
Paul Scherrer Institut, CH 5232 Villigen PSI, Switzerland
W. H. Breunlich, M. Cargnelli, B. Gartner, R. King, B. Lauss, J. Marton, H. Zmeskal
Institut für Mittelenergiephysik, Wien, Oesterreichische Akademie der Wissenschaften
F. Kottmann
Institut für Teilchenphysik, ETH Zürich, CH-8093 Zürich
G. Rasche
Institut für Theoretische Physik, Universität Zürich, CH-8057 Zürich

Abstract

We propose to measure the strong interaction width and shift of the ground state of pionic hydrogen in order to determine the pion-nucleon scattering lengths for both isospin components a^+ and a^- with a relative accuracy of better than 10^{-2}. The scattering length a^- extracted from the width measurement has a direct relation to the pion–nucleon coupling constant and can be directly compared with predictions of chiral perturbation theory. Systematic errors of the width measurement caused by Doppler broadening can be corrected by comparing simultaneous experiments with pionic and muonic hydrogen atoms.

Contents

1 Beam requirements.

1.1 Experimental area: $\pi E5$

Required beam properties:

- We request negative pions of a momentum of 100 MeV/c with a momentum width of 7%.
- The beam intensity should be maximum: i.e. 1.5 mA proton current with full length of target E.

The cyclotron trapII is required for the whole time of the experiment.

1.2 Duration of the experiment.

- The preparation outside the $\pi E5$ area (NA hall) will take several months for calibration of the crystal spectrometer.
- The preparation time inside the pion area will be typically a week before each measuring pweriod.
- We ask for about 2.5 months/year of beam time in the $\pi E5$ area for the years 1999-2002.

1.3 Special conditions.

The experiment needs a preparatory phase for the calibration of the crystal spectrometer. It is proposed to perform measurements with an ECR source in the NA hall. We ask therefore for a place in the NA hall to set up the whole equipment. We also ask for laboratory space inside the WMHA.
For the experiment with pions we should have our electronics hut as near to the experiment as possible.

2 Declaration sheet for hazardous equipment.

3 Introduction.

The present proposal deals with a high precision study of strong interaction phenomena in the pionic hydrogen atom. It aims at concluding a series of experiments which have shown an increasing level of sophistication and precision [1, 2, 3, 4].
The pionic hydrogen atom is dominated by the electromagnetic interaction of its constituents. Their strong interaction is only effective in case the wave functions of pions and protons significantly overlap, i.e. in the s–states, which results in a broadening and shift of the s–states. The electromagnetic binding energy of the 1s state is E_{1s}=3238 eV whereas the strong interaction shift ϵ of the ground state is about 7 eV (attractive i.e. the $1s$ state is stronger bound) and the width Γ amounts to about 1 eV only. The quantities which are finally extracted from the shift and width measurement are the isospin scattering lengths in the pion–nucleon system for both isospins. The relations of the measured quantities to the hadronic scattering lengths a^h describing the $\pi^- p \to \pi^- p$ and the $\pi^- p \to \pi^0 n$ processes respectively are given by the Deser–type formulae [5, 6]:

$$\frac{\varepsilon_{1s}}{E_{1s}} = -4 \cdot \frac{1}{r_B} a^h_{\pi^- p \to \pi^- p}(1 + \delta_\varepsilon) \tag{1}$$

$$\frac{\Gamma_{1s}}{E_{1s}} = 8\frac{Q_0}{r_B}(1 + \frac{1}{P})(a^h_{\pi^- p \to \pi^0 n}(1 + \delta_\Gamma))^2 \tag{2}$$

Here r_B is the Bohr radius of the pionic hydrogen atom with r_B= $222.56 fm$, δ_ϵ, δ_Γ are electromagnetic corrections, Q_0= $0.142 fm^{-1}$ is a kinematical factor and $P = 1.546 \pm 0.009$ is the Panofsky ratio [8]. The resolution of a dedicated crystal spectrometer can reach a value of $\sim 10^{-4}$ which permits a determination of shift and width with a relative precision of better than 1% provided enough statistics has been collected and the response function of the detection system is well known. The method is limited by the knowledge of the factors contributing to the Deser formulae and additional corrections which will be discussed later. The Panofsky ratio is known with an accuracy of about $5 \cdot 10^{-3}$ which is also the accuracy at which the electromagnetic corrections are known.
Some unique features of the exotic atom's method should be recalled:

- The electromagnetic interaction in exotic hydrogen atoms is well understood. The binding energies are known with an accuracy of $3 \cdot 10^{-6}$, which is the precision in the mass of the pion [9]. Any deviation caused by another interaction can therefore be studied with high precision.

- Conventional scattering experiments are restricted to energies above about 10 MeV [10, 27] and have to rely on an extrapolation to zero energy in order to extract the scattering lengths. The exotic atom's method, however, directly measures linear combinations of the isospin separated scattering lengths [5] at almost zero energies. Most important is the fact that the exotic atom's method offers the highest intrinsic accuracy of all methods.

- Pionic hydrogen is one of the simplest hadronic systems bound electromagnetically and is therefore ideally suited for a study of strong interaction. The even simpler $\pi^+\pi^-$atoms

are at the moment subject of a challenging proposal at CERN [7]. They are difficult to produce and will not allow for a longer time to perform high precision studies comparable to the present proposal.

On the theoretical side the description of the pion–nucleon system is considered to be a fundamental problem of QCD. The understanding of strong interaction in the confinement regime has advanced recently, as Chiral Perturbation Theory ($CHPT$) was developed to perform calculations at low energies [11, 12, 13]. It offers the method to describe the pion–nucleon system quantitatively especially at low energy and allows to calculate certain combinations of scattering lengths with percent accuracy using all available experimental information.
The proposed experiment requires the cyclotron trap II at the πE5 channel with the highest possible beam intensity. The X–rays emitted from the pionic hydrogen atom will be energy–analysed by a high resolution crystal spectroscopy using spherically bent Bragg crystals. In order to extract a line width with a relative accuracy of better than one percent the response function of the crystal spectrometer must be known with sufficient precision. Therefore the resolution and the response function of the Bragg crystals will be optimized and measured off beam with X–rays of single electron ions from an ECR (Electron Cyclotron Resonance) source. The response function of the crystals will then be surveyed during measurement with X–rays of well defined line shape and energy from specially chosen pionic and muonic atoms which are not influenced by any broadening mechanism.
The required good knowledge of the response function alone is not sufficient to perform a successful determination of the width because the X-ray transitions will not only be broadened by strong interaction but also by Doppler effect. The pionic hydrogen atom changes its velocity during the cascade as its excitation energy can be transformed into kinetic energy (Coulomb deexcitation). The cross section for this process and therefore the development of the kinetic energy during the cascade is presently not well known. A possible way to assess the influence of Doppler broadening is to determine the kinetic energy distribution in muonic hydrogen which is a very similar system but not affected by strong interaction. The spectrum of the kinetic energies and hence the Doppler broadening here is rather similar to the pionic case as the reduced mass of the muonic hydrogen atom is only 21% smaller than the reduced mass of the pionic hydrogen atom. Compared to pions muons have a spin different from zero leading to a hyperfine structure of the atomic levels. The cascade processes leading to an acceleration of the exotic hydrogen atoms are not influenced by this fact as they occur at levels where the hyperfine splitting can be neglected. Therefore a high resolution spectroscopy of muonic hydrogen transitions allows one to determine the different contributions of the Coulomb deexcitation in this system. This knowledge can be transferred to pionic hydrogen and will serve as input for the fitting of the corresponding pionic hydrogen spectra.
The measurement of muonic hydrogen is in the present context considered as a necessary calibration. It can be stated, however, that a high resolution crystal spectrometry of muonic hydrogen unambiguously determines the kinetic energies developing during the cascade and thus will solve a long standing problem of the theory of cascade in exotic atoms.

4 Theoretical Background.

4.1 Strong interaction

Quantum Chromodynamics (QCD) is the theory of strong interactions and one of the components of the $SU(3) \times SU(2) \times U(1)$ Standard Model. For the benefits of the reader we remind briefly some of its basic features. QCD is the gauge field theory that describes the interactions of colored fermionic fields (quarks) and non-Abelian colored gauge fields (gluons). The (local) gauge transformations form the group $SU(3)$ (color group) with the quarks and gluons belonging to the fundamental (triplet) and adjoint (octet) representations of the color group . The gluons mediate the interaction between the quarks, and in addition, due to the non-Abelian character of QCD, the gluons also interact with each other. The strength of interaction between colored objects is scale dependent. The renormalized QCD coupling constant is small at high energy (asymptotic freedom); in this domain the fundamental fields of QCD, quarks and gluons, can be probed experimentally in a direct way, and high-precision theoretical predictions using perturbation theory can be confirmed. On the other hand, the attraction between two colored objects grows with increasing distance, that leads to the confinement of quarks and gluons, so that only colorless particles ($SU(3)$ singlets) manifest themselves as asymptotic states. At low energy the color degrees of freedom are not directly observable. In this case the hadron dynamics is equivalent to an *effective* field theory of colorless hadrons.

4.1.1 QCD and chiral perturbation theory

The QCD Lagrangian has the form

$$\begin{aligned}
\mathcal{L}_{QCD} &= \mathcal{L}_g + \mathcal{L}_q + \mathcal{L}_m \\
\mathcal{L}_g &= -\frac{1}{4g^2}\mathrm{Tr}\,(G_{\mu\nu}G^{\mu\nu}) \\
\mathcal{L}_q &= \sum_{f=1}^{N_f} \bar{\psi}_f i D_\mu \gamma^\mu \psi_f \\
\mathcal{L}_m &= \sum_{f=1}^{N_f} m_f \bar{\psi}_f \psi_f \\
D_\mu &= \partial_\mu - igA_\mu \\
G_{\mu\nu} &= [D_\mu, D_\nu]
\end{aligned}$$

where A_μ is the gluon field, ψ_f is the quark field of the f-th flavor ($\psi_f = (u, d, c, s, t, b)$), D_μ is the covariant derivative, $G_{\mu\nu}$ is the field strength tensor, and g is the color charge. The term $\mathcal{L}_g$ describes pure gluon dynamics, the term $\mathcal{L}_q$ corresponds to the quark kinetic energy and quark-gluon interaction, and the term $\mathcal{L}_m$ is responsible for the quark masses. In the massless limit, the QCD Lagrangian ($\mathcal{L}_g + \mathcal{L}_q$) depends on only one dimensionless parameter g. At the same time the strong coupling constant $\alpha_s(\mu)$ becomes scale dependent due to renormalization. The scale parameter of QCD is determined from experiment. Provided the quarks are massless, the chirality (helicity) of a quark is conserved and the QCD Lagrangian is symmetric with respect to rotations in the flavor space independently for right- and left-handed quarks, thus the massless QCD has the global symmetry described by the group $SU(N_F)_R \times SU(N_F)_L$. While the Lagrangian is chirally symmetric, the ground state of the

massless QCD (vacuum) does not have the same property because the chiral symmetry is spontaneously broken: The characteristic feature of this spontaneous symmetry breaking is the emergence of massless pseudoscalar particles (Goldstone bosons) (in the case of two flavors, $N_F = 2$, they correspond to the triplet of pions). The essence of the chiral perturbation theory is to consider the quark mass term $\mathcal{L}_m$ as a perturbation [13]. The mass term explicitly breaks the chiral symmetry, so that the Goldstone bosons get nonzero masses, and in the leading order the pion mass squared is proportional to the quark mass: Chiral perturbation theory (CHPT) is an *effective* field theory constructed as an expansion in momenta and masses of physical particles, which are considered to be small on a hadronic scale of about 1 GeV. This approach is extended in baryon chiral perturbation theory, so that the meson interaction with "heavy" baryons can be treated as well [12]. Along this way the current algebra derived long time ago gets a modern framework. The near-threshold pion-nucleon scattering amplitude is of great interest for chiral perturbation theory. In particular, the isospin-even part of the πN scattering amplitude at the (unphysical) Cheng-Dashen point ($\nu = (s-u) = 0$, $t = 2m_\pi^2$) is related to the sigma term which describes the measure of the explicit chiral symmetry breaking:

$$\sigma = \frac{\hat{m}}{2M}\langle p|\bar{u}u + \bar{d}d|p\rangle \tag{3}$$

where $|p\rangle$ denotes the proton state, M is the proton mass, and $\hat{m} = (m_u + m_d)/2$ is the average mass of the u and d quarks. On the other hand, the sigma term is related to the observed $SU(3)$-breaking mass differences in the baryon octet and the strangeness content of the nucleon. For detailed discussion of these relations we refer to [11, 14, 15, 16] and references therein. Since chiral perturbation theory is built as a low-energy expansion, it naturally concerns low energy parameters, such as scattering lengths and ranges, which provide very important experimental input determining the parameters of CHPT. Precise experimental data are therefore crucial for a critical test of the predicting power of chiral perturbation theory. For a discussion of these topics we refer to [17] and references therein.

4.1.2 πN Scattering length

Before going into a discussion of the present knowledge of the πN scattering length, we briefly introduce different notations existing in the literature, which are relevant for the pionic hydrogen problem. With I denoting the isospin of the πN system, the scattering lengths a^h can be represented by linear combinations of the scattering lengths a_I as

$$a^h_{\pi^- p\to\pi^- p} = \frac{2a_{1/2} + a_{3/2}}{3} \tag{4}$$

$$a^h_{\pi^- p\to\pi^0 n} = \frac{\sqrt{2}(a_{1/2} - a_{3/2})}{3} \tag{5}$$

Instead of $a_{1/2}$ and $a_{3/2}$ sometimes the notations a_1 and a_3 are used. The scattering lengths a_I are related to the *isospin-even* and *isospin-odd* scattering length, a^+ and a^-, respectively, as follows

$$a^+ = \frac{a_{1/2} + 2a_{3/2}}{3} \tag{6}$$

$$a^- = \frac{a_{1/2} - a_{3/2}}{3}. \tag{7}$$

Reference	a^+	a^-	$(a^+ + a^-)$
Experiment			
Data Analysis			
$\pi^- p$ atom [19]	-0.0037(50)	0.0920(42)	0.0883(8)
Koch [21]			0.083(4)
KH83 [25]	-0.0097(17)	0.0913(17)	
$\pi^- p \to \gamma n$ [27]		0.0842(21)	
$\gamma p \to \pi^0 p$ [25]		0.0877(16)	
SAID [28]	-0.000(1)	0.088(1)	0.088(1)
Theory			
Weinberg [29], Tomozawa [30]	0.	0.079	0.079
Bernard *et al.* [31]		0.0916(15)	
Bernard *et al.* [32]		0.092(4)	
Mojžiš[34]	-0.0098(130)	0.0935(140)	
Goudsmit *et al.* [35]	-0.003(4)	0.083(1)	

Table 1: The πN scattering lengths (in units m_π^{-1}).

The present knowledge of the values for the scattering lengths a^+, a^-, and $a^h_{\pi^- p \to \pi^- p} = (a^+ + a^-)$ is shown in Table 1.
The measurements of the hadronic shift in the $\pi^- p$ atom with the relative accuracy of about 1% give the most precise value of the linear combination $(a^+ + a^-)$ and can be used to constrain the phase shift analysis of the scattering data. On the other hand, the current accuracy of the widths measurements of about 10% is not sufficient for extracting a precise value of a^-. This situation is in striking contrast with the theory where the isospin-odd scattering length a^- is relatively better determined than the isospin-even scattering length a^+, because large cancellations occur for the latter, so that the result is sensitive to certain theoretical parameters. A better experimental determination of the scattering length a^- will be of big importance for reducing this theoretical uncertainty. Another problem that requires precision experimental data is related to the isospin symmetry breaking due to the mass difference of the up and the down quarks (see [17] and references therein).

4.1.3 πN coupling constant

Another motivation for a better direct determination of the pion-nucleon scattering lengths is connected to the πN coupling constant $f_{\pi N}$. The Goldberger-Miyazawa-Oehme (GMO) sum rule [18], which is obtained from a forward dispersion relation for the isospin-odd πN scattering amplitude, provides a relation between the scattering length a^- and the πN coupling constant $f^2_{\pi N}$:

$$(1 + \frac{m_\pi}{M})\,\frac{a^-}{m_\pi} = \frac{2 f^2_{\pi N}}{m^2_\pi - (m^2_\pi/2M)^2} + J \tag{8}$$

$$J = \frac{1}{2\pi^2}\int_0^\infty \frac{\sigma^-(k)}{\omega(k)}\,dk \approx -0.053 m_\pi^{-2} \tag{9}$$

Here k and $\omega(k)$ are the incident pion momentum and energy, and $\sigma^-(k) = (\sigma^{tot}(\pi^- p) - \sigma^{tot}(\pi^+ p))/2$ is the isospin-odd total cross section. The integral (9) is known with an accuracy

of the order of 1% (see [36, 37, 38] and references therein). Therefore the determination of the width $\Gamma_{1S}(\pi^- p)$ with one percent accuracy offers the possibility to determine the pion-nucleon coupling with an accuracy of better than 1%. An immediate application is an evaluation of the Goldberger-Treiman discrepancy [39, 40] which accounts for a small correction to the Goldberger-Treiman relation

$$f_{\pi N}^2 \quad = \quad \frac{m_\pi g_A^2}{16\pi F_\pi^2} = 0.072 \tag{10}$$

where g_A is the axial-vector coupling constant and F_π is the weak pion decay constant.

4.1.4 Electromagnetic corrections.

Extending the pioneering work of Rasche and Woolcock [6] the electromagnetic corrections to the pion nucleon scattering lengths have been calculated in a recent publication [42] with a relativistic two channel approach. The results for the correction to the shift measurement δ_ε and the width measurement δ_Γ are δ_ε=-(2.1$\pm$0.5)$\times 10^{-2}$ and δ_Γ=-(1.3$\pm$0.5)$\times 10^{-2}$, respectively. The uncertainty of 5×10^{-3} together with the error in the Panofsky ratio can be considered as the final accuracy the experiment should reach.

4.2 Atomic cascade.

4.2.1 The different cascade processes.

Exotic hydrogen atoms exhibit cascade features entirely different from other exotic atoms [44]. They do not possess electrons and therefore internal Auger effect is excluded as deexcitation mechanism. The main collisional deexcitation mechanism is the external Auger effect

$$(\pi^- p)_i + H_2 \rightarrow (\pi^- p)_f + e^- + H_2^+.$$

Because of their neutrality the $\pi^- p$ atoms are not hindered by a Coulomb barrier to closely approach a hydrogen nucleus of the surrounding medium. This allows fast transitions between different l–levels of the same principal quantum number n by Stark mixing:

$$(\pi^- p)_{nl} + H \rightarrow (\pi^- p)_{nl'} + H.$$

The most influential process for the proposed experiment is the Coulomb deexcitation:

$$(\pi^- p)_i + p \rightarrow (\pi^- p)_f + p$$

with $n_f < n_i$,in which the exotic hydrogen atom gains nearly half of the transition energy as kinetic energy. The exotic atom is decelerated in elastic scattering

$$(\pi^- p)_n + H \rightarrow (\pi^- p)_n + H$$

where the kinetic energy is distributed between the collision partners. The above-mentioned collisional processes depend on the target density. Media independent processes include radiative deexcitation

$$(\pi^- p)_i \rightarrow (\pi^- p)_f + \gamma$$

process	energy	density	Refs
Radiative	no	no	[43]
Nuclear reaction	no	no	[21]
External Auger effect	no	linear	[44]
Stark mixing	weak	linear	[44, 45]
Coulomb deexcitation	$\sim \frac{1}{\sqrt{T}}$	linear	[46, 53, 47, 48, 49]
Elastic scattering	$\sim \frac{1}{\sqrt{T}}$	linear	[50, 51, 52]

Table 2: Different processes influencing the cascade together with their dependence on kinetic energy T of the $\pi^- p$ atom and the target pressure.

and the nuclear reactions

$$(\pi^- p)_{ns} \rightarrow \pi^0 + n,$$

$$(\pi^- p)_{ns} \rightarrow \gamma + n.$$

The list of the different processes occuring in the pionic hydrogen and their dependencies on pressure and kinetic energy of the pionic hydrogen atom is given in Table 2.
The cascade of muonic hydrogen involves the same processes apart from the nuclear reactions. Muon decay or capture are very slow and do not play any role at excited levels at the pressures involved. The same argument holds for the influence of the spin of the muon as well.

4.2.2 Present knowledge of Coulomb deexcitation.

The proposed experiment depends on a good knowledge of the $(\pi^- p)$ kinetic energy distribution at the instant of the X–ray transitions. Recent experiments [54, 55, 65] with liquid hydrogen using a neutron time–of–flight (nToF) method found a large fraction of "high energy" ($\gg 1eV$) πp atoms at the states where the pion capture occurs. Experiments in the gaseous state at $40bar$ support the result of the experiments with liquid hydrogen [66]. The data obtained with the nToF method allow to calculate the kinetic energy distribution at the instant of nuclear reaction in a model independent way as shown in Appendix 2. Also measurements with muonic hydrogen at pressures in the 100 mbar region show a significant high kinetic energy component [67].
This high energy component is attributed to the Coulomb deexcitation

$$(\pi^- p)_i + p \rightarrow (\pi^- p)_f + p$$

in which the transition energy is transferred into the kinetic energy of the πp atom and the proton. The rates of the Coulomb deexcitation have been calculated by several groups. The results differ by more than one order of magnitude [46, 47, 48, 49, 53] . This uncertainty can be greatly reduced by fitting the experimental data with the atomic cascade model, see [56, 52] and references therein. The recent experimental observations of high energy components in the $\pi^- p$ and $\mu^- p$ kinetic energy distributions stimulated further theoretical studies of deceleration and acceleration mechanisms [57, 58, 59]. We plan to upgrade our cascade model by including the results of these new calculations and using a more accurate model of the Stark mixing with the strong interaction effects directly taken into account [60]. We also expect to benefit from

Transition	$1bar$		$15bar$	
	$\pi^- p$	$\mu^- p$	$\pi^- p$	$\mu^- p$
$2 \rightarrow 1$	6.5	47.6	3.4	55.4
$3 \rightarrow 1$	2.7	21.0	2.9	36.6
$4 \rightarrow 1$	3.5	22.1	2.0	7.0
$rest \rightarrow 1$	4.4	9.3	0.6	1.0
Total yield	17	100	8.9	99.9

Table 3: Calculated absolute yields (%) of muonic and pionic hydrogen K–transition.

the final results of the measurements of the $\pi^- p$ kinetic energy distribution at the instant of nuclear reaction [61, 66], which can be extracted in a model independent way (see Appendix 2).
A significant improvement can further be achieved by performing a combined fit of the $\pi^- p$ and $\mu^- p$ data with the cascade model. The atomic cascade in the $\mu^- p$ atom does not involve any nuclear reaction while all the deexcitation processes are very similar to the $\pi^- p$ case. As a result, the cascade in the $\mu^- p$ atom allows to study the Coulomb deexcitation directly by observing the Doppler broadening of the X–ray lines [62].
The measurement of the Coulomb deexcitation via the observation of the Doppler broadening of muonic hydrogen X-rays is therefore an essential part of the planned experiment.

4.2.3 Yields of X–ray transitions in muonic and pionic hydrogen and corresponding distributions of kinetic energies.

The intensities of the X–ray yields in the $\pi^- p$ and $\mu^- p$ atoms calculated with the Monte Carlo code [62, 56] are shown in Table 3. The cascade model used is in good agreement with the experimental data on the $\mu^- p$ X–ray yields [63] and in fair agreement with $\pi^- p$ data [56, 64]. Important for the proposed experiment is the fact that the muonic $2 \rightarrow 1$ and $3 \rightarrow 1$ transitions are about an order of magnitude stronger than the corresponding pionic transitions. This compensates the lower stop efficiency for muons. An extension of the measurement to the $4 \rightarrow 1$ transition can also be considered; the intensity, however, decreases significantly for higher pressures. In addition the Bragg angles are becoming small and make this transition unfavorable. Rate estimates based on the yields of Table 3 are given in chapter 3.6.
In Figures 1 -4 calculated distributions of kinetic energies are shown for a pressure of 15 bar for the exotic hydrogen atoms at the instant of the $2 \rightarrow 1$ and the $3 \rightarrow 1$ transition. (We always give the values for the pressures at a temperature of 293K.) The influence of these distributions on the form of the X–ray lines is depicted in Fig. 8-9.

4.2.4 Combined analysis of $\mu^- p$ and $\pi^- p$ data.

The comparison of the calculated Doppler broadening of the $\mu^- p$ $K\alpha$ and $K\beta$ lines with the result of the proposed experiment will allow us to perform a fine tuning of the Coulomb and deceleration rates. The $\pi^- p$ data on the kinetic energy distribution obtained with the nToF method will also be used for this goal. By transferring this information into the $\pi^- p$ part of the cascade calculations we are confident that the current uncertainties in the calculated energy distributions of the $\pi^- p$ atom at the instant of the X–ray transitions will be reduced

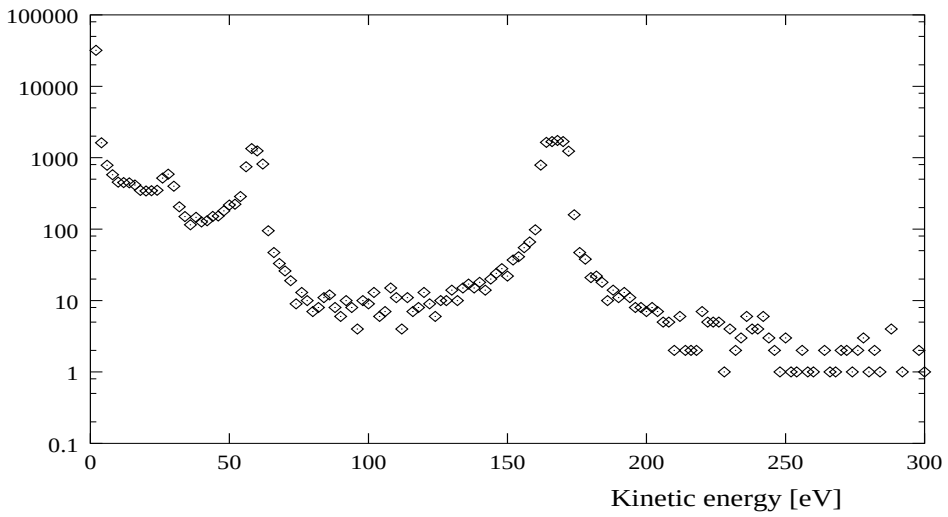

Figure 1: The calculated spectrum of the kinetic energy of the muonic hydrogen atom at the instant of the $2 \to 1$ transition. The pressure is $15bar$, the total number of $\mu^- p$ atoms is 10^5.

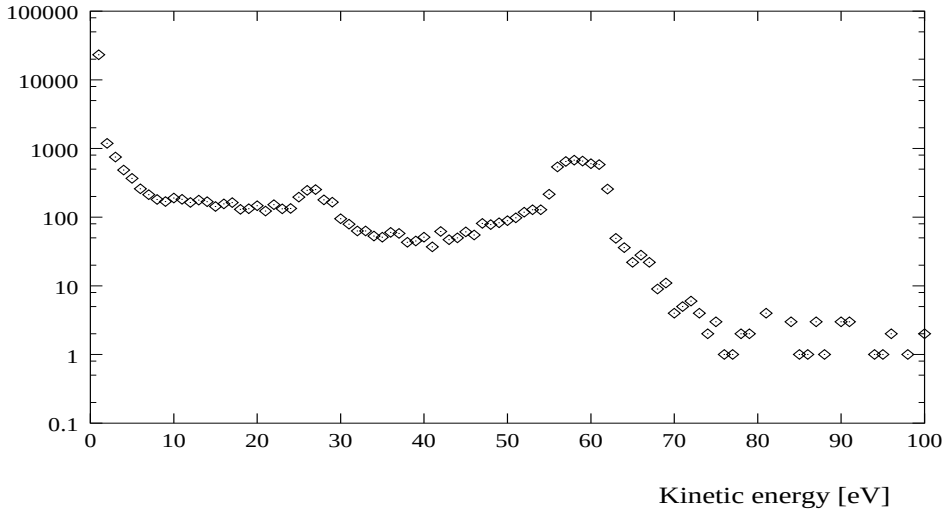

Figure 2: The calculated spectrum of the kinetic energy of the muonic hydrogen atom at the instant of the $3 \to 1$ transition. The pressure is $15bar$, the total number of $\mu^- p$ atoms is 10^5.

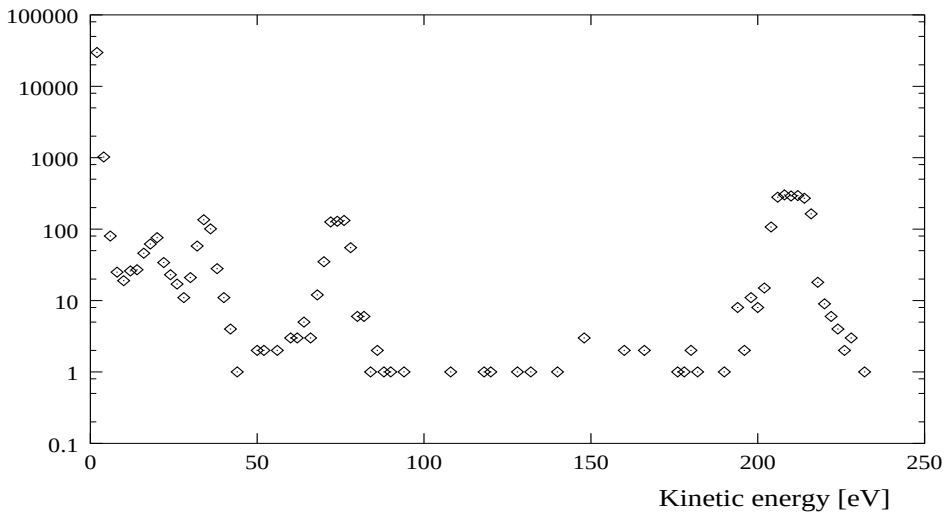

Figure 3: The calculated spectrum of the kinetic energy of the pionic hydrogen atom at the instant of the $2 \to 1$ transition. The pressure is $15bar$, the total number of $\pi^- p$ atoms is 10^6.

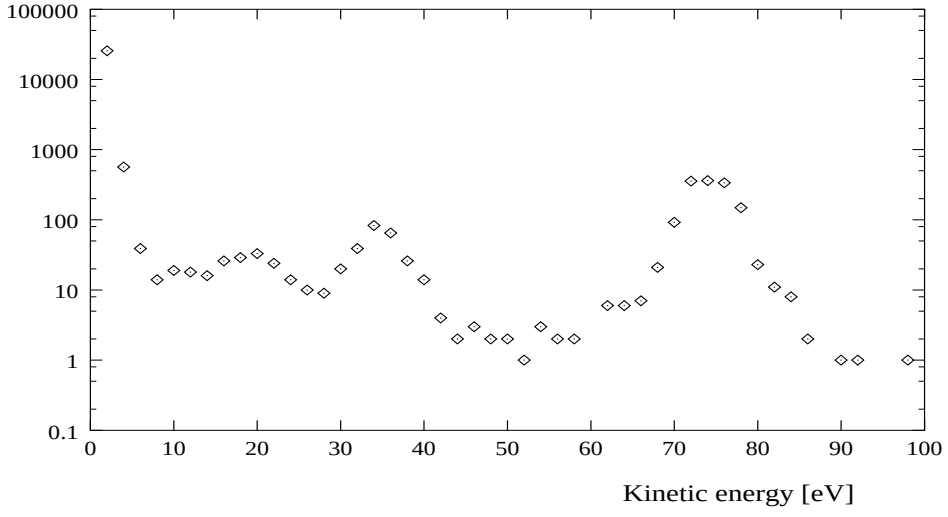

Figure 4: The calculated spectrum of the kinetic energy of the pionic hydrogen atom at the instant of the $3 \to 1$ transition. The pressure is $15bar$, the total number of $\pi^- p$ atoms is 10^6.

to the level allowing to predict the Doppler broadening correction to the X–ray lines profile with an error of better than 1% in the hadronic width.

5 Experimental method.

5.1 First considerations.

The goal of the experiment is to measure the strong interaction ground state shift and width in pionic hydrogen with a high resolution crystal spectrometer. The experiment will concentrate on the improvement of the precision of the width measurement by one order of magnitude. The knowledge of the value for the shift will be improved also by almost an order of magnitude because of better statistics and by extensive studies of sources of systematic errors like the pressure dependence of the measured shift.
It will be demonstrated below that the combination of the cyclotron trap II and spherically bent crystals with an extended CCD detector provides a sufficient resolution with acceptable rates and measuring times.
The main difficulty in the experiment is to quantify the influence of Doppler broadening on the line shape caused by Coulomb deexcitation. One way to solve this problem would be to perform the measurement with transitions from high levels $n > 10$ where no sizable Coulomb acceleration can occur. Unfortunately the yield of these transtions is too low for a high statistics study of the line broadening. Also using low pressures will not eliminate the Doppler broadening completely as recent experiments [68] show the Coulomb acceleration still exists in the mbar region. The high statistics experiment is thus restricted to pressures $> 5bar$ and to the transitions from $n < 5$ for pionic hydrogen and $n < 4$ for muonic hydrogen because of intensity reasons.
The present experiment will be performed with the $2 \rightarrow 1$ and the $3 \rightarrow 1$ transitions in pionic hydrogen. The corresponding transitions in muonic hydrogen will be measured simultaneously with a special arrangement of two SiO_2 crystals working with different reflection planes. This saves beam time and, more importantly guarantees that no systematic error occurs because of change of experimental parameters. The effect of the Doppler broadening as determined from the muonic measurement will deliver the input parameters for the fitting of the pionic lines as discussed in chapter 2.2.4. The soundness of this procedure is then checked by comparing the results for the width extracted from both the $2 \rightarrow 1$ and the $3 \rightarrow 1$ transitions measured at different pressures, typically between $5bar$ and $40bar$. **The strong interaction width must be independent of the transition line and the pressure if all corrections have been treated properly .** This will also allow us to check that other minor effects like the X-ray broadening due to transitions during the Stark collisions do not affect the accuracy of the measurement.
The measurement of higher transitions in pionic hydrogen, like the $4 \rightarrow 1$ transition and transitions at the series limit, are presently not considered as they require different Bragg crystals, but they could be the subject of a following proposal.
As we heavily rely on the two crystal method for a simultaneous measurement of pionic and muonic atoms, we propose to do extensive preparatory experiments with electronic X–rays before setting up the experiment at the pion beam. These experiments are planned to take place in the NA hall at PSI. They will use an ECR source and fluorescence X–rays as mentioned in chapter 4.1. The corresponding experimental set–up will be described in chapter 6.1.

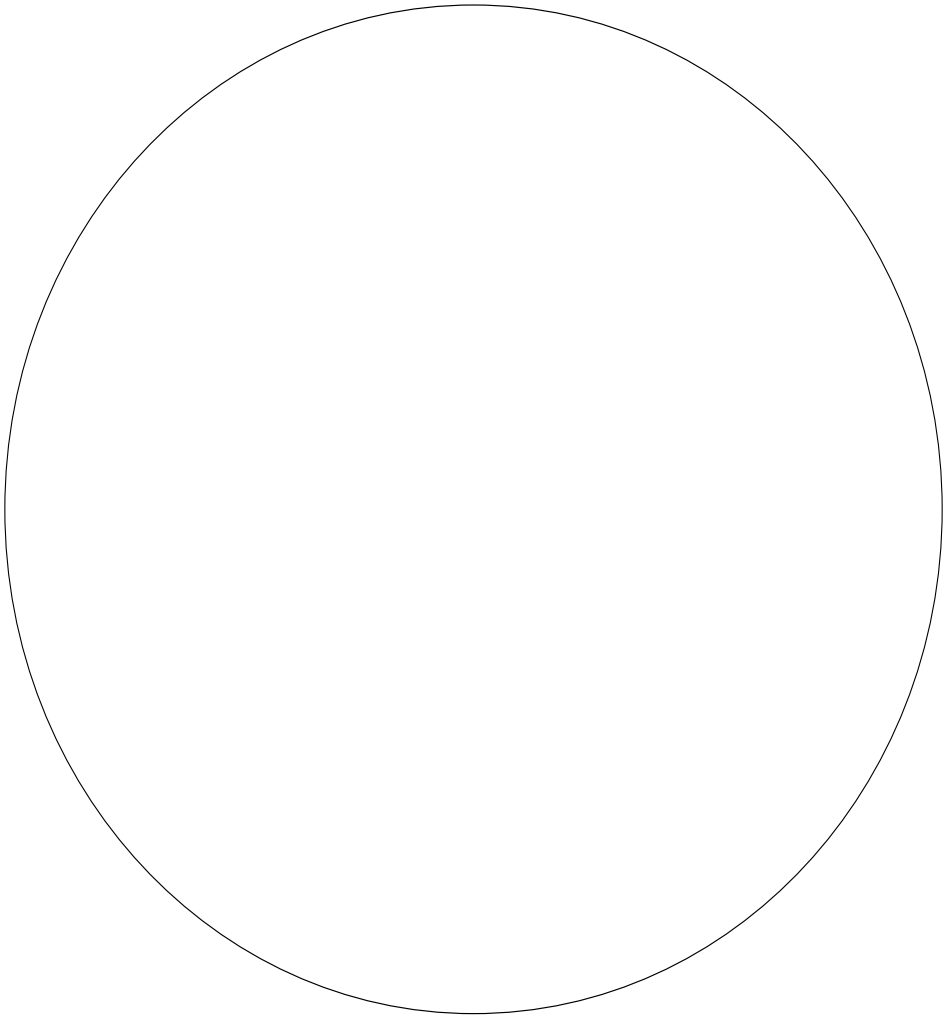

Figure 5: Set–up of the experiment at the $\pi E5$ channel at PSI. A very similar set-up will also be used outside the pion area for the tuning of the spectrometer with X-rays from an ECR-source.

5.2 Beam and cyclotron trap.

The experiment will be set up at the πE5 channel. A sketch of the set–up is given in Figure 5. The different parts of the experimental set–up and their role in the experiment will be described below.
A proton beam current of 1.5 mA and the full thickness of target E are required and are taken as basis of our rate estimates. The high beam current can also be fully exploited as the experiment is not rate limited. The beam momentum is 110 MeV/c . The cyclotron trap will be tuned to a momentum of accepted particles of about 82 MeV/c. The particles will be stopped in a thin walled (Kapton) cylindrical gas target (diameter 60 mm, length 200 mm) with the cylinder axis coinciding with the axis of the magnetic field. The particle density of the target gas corresponds to a pressure range from $\cong$1 bar to $\cong$40 bar at room temperature. The required particle densities can be reached by cooling the target. In order to optimize the stops in the target gas as compared to the ones in the walls the thickness of the cylinder wall

is restricted to a thickness of $\leq$50 μm of Kapton. The X–ray window at the front plane of the target cylinder will be made out of $5\mu m$ Mylar supported by a stainless steel grid.
The magnetic field configuration and the deceleration scheme of the cyclotron trap has been optimized with tracking calculations. These calculations predicted a rate of about $3 \cdot 10^5$ pion stops for hydrogen at a pressure of 1 bar. In preparation of the present proposal a stop rate for pions has been determined in deuterium gas at a pressure of $2.5bar$ measuring the pionic $2 \rightarrow 1$ transition (see chapter 3.3 and Figure 6). It can be safely assumed that the pion stop rate is proportional to the particle density in the pressure region considered and that there is no difference in stopping power between the two hydrogen isotopes. The measured number of about 10^6 stopped pions agrees well with the value given above if one scales the pressures. Muons will be produced by decays of pions orbiting inside the cyclotron trap. This results in a muon stop rate which is one order of magnitude smaller than the pion stop rate. This reduction is compensated, however, by a higher X–ray yields in the $\mu^- p$ atoms.
It is foreseen to shim the so–called form iron of the cyclotron trap in order to increase the injection efficiency by about a factor of two with a corresponding gain in stopping power.

5.3 The crystal spectrometer.

The crystal spectrometer combined with the CCD detectors serves to measure angles with optimized resolution and luminosity. It is planned to use a very similar arrangement as in a recent test measurement where the pionic deuterium $2 \rightarrow 1$ transition has been measured at a pressure of 2.5 bar. This measurement serves as a basis for the discussion of this proposal in terms of resolution and rates. The corresponding spectrum obtained with a Si (111) crystal is shown in Fig. 6.
The rate of measured deuterium X–rays is $(53 \pm 2)/h$ for a continuously running machine at 1.5 mA. The peak/background ratio is 30/1. This result shows a substantial improvement compared to a recent measurement of pionic deuterium X–rays at PSI [69]. For the proposed experiment SiO_2 crystals will be preferentially used as will be explained below. These crystals have a factor of 2 -5 lower reflectivities. With vertically bigger CCD detectors and an improved stop efficiency this loss will be overcompensated. The excellent peak/background ratio can be improved further by carefully tailoring a shielding around the path of the X–rays thus reducing the background and by enhancing the stop rate in hydrogen. An improvement factor of about three can safely be expected. Before going into more technical details the gross features of crystal spectroscopy together with some basic relations are introduced.

5.3.1 Bragg spectroscopy and available crystals.

The energy E of X–rays emitted from the target region is analyzed by Bragg reflection from spherically bent single crystals. These are mounted in the so–called Johann geometry [70]. The energy analysis relies on the Bragg reflection condition

$$n \cdot \lambda = 2 \cdot d \cdot sin\Theta_B \tag{11}$$

with

$$\lambda = 2\pi \frac{\hbar c}{E}. \tag{12}$$

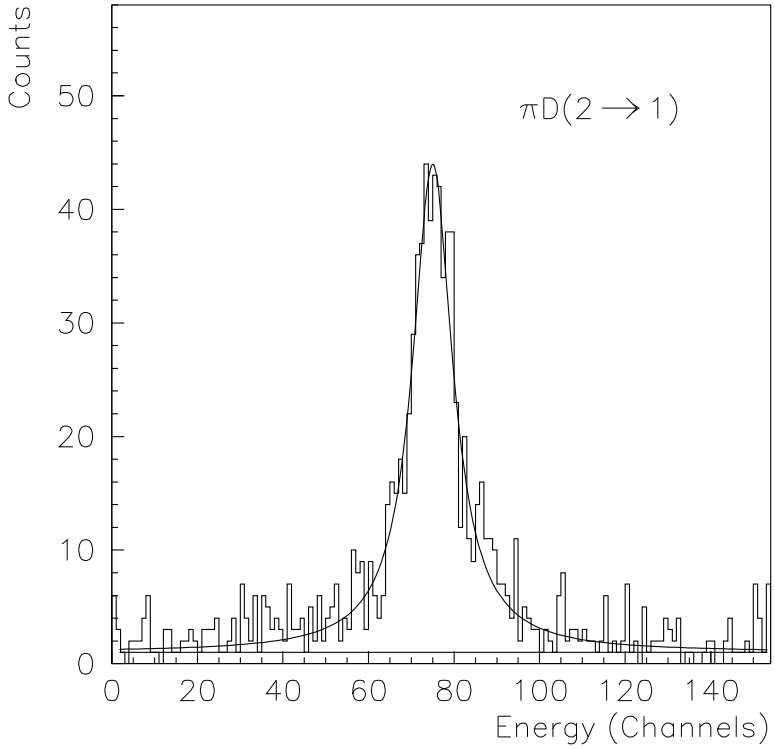

Figure 6: Pionic deuterium measured with a Si 111 spherically bent crystal.

Crystal	plane	2d[nm] at $22.5^0 C$	Energy[eV]		Temp. coeff.
			$\Theta_B = 90^0$	$\Theta_B = 65^0$	
SiO_2	100	0.85110(4) [71]	1457	1607	$1.4 \cdot 10^{-5}/K$
SiO_2	10.1	0.66862(4) [71]	1854	2045	$1.4 \cdot 10^{-5}/K$
Si	111	0.62712016(18) [72]	1977	2181	$2.6 \cdot 10^{-6}/K$

Table 4: Physical properties of the Bragg crystals available for the experiment.

The Bragg condition corresponds to the coherent superposition of X–rays of wavelength λ reflected from lattice planes with a spacing of d into a direction given by the reflection angle Θ_B, n is the order of reflection. In the following we only consider Bragg reflection of the first order.
The angular width of reflected monoenergetic X–rays determines the intrinsic energy resolution. It depends on the crystal properties for a given wavelength. More information about the imaging properties of bent crystals and the facts limiting the resolution of bent crystal spectroscopy are given in Appendix 1.
The single crystals with best known properties for our energy region are Si and SiO_2 (quartz) crystals. For the energy region below $3.3keV$, which is about the series limit for the pionic hydrogen K transitions, only the 111 lattice plane for Si and the 100 and 10.1 lattice planes for quartz can be used. Some properties of these crystals are listed in Table 4.
With quartz 100 it is also possible to measure the muonic $K\alpha$ transition. All these crystals cut to the appropiate planes are at the disposal of the experiment. Their geometrical form is a circular disk with a thickness of $0.3mm$ and a diameter of $100mm$. In order to achieve spatial focussing they are spherically bent by mounting them on a concave glass lens. The radius of curvature is $R_c = 2985.4mm$ for three available Si (111) crystals and three SiO_2(100) crystals. The two available SiO_2 (10.1) crystals are presently still mounted with $R_c = 2660mm$ which is foreseen to be changed. As the measurement aims at a final accuracy in the energy determination of about 10^{-6} the Bragg crystals have to be temperature stabilized.

5.3.2 Transition energies of pionic hydrogen and Bragg angles.

The energies of the muonic and pionic hydrogen Lyman X–rays vary between 1896 and 3244 eV. In Table 5 the transition energies for pionic and muonic hydrogen are given together with the relevant crystal plane and reflection angles.
Not all Bragg angles which are listed in Table 5 are suited for the experiment. Their choice is limited by the following considerations. First, the energy resolution as derived from the Bragg relation varies as $cot\Theta_B$. The broadening (see Appendix 1) which is caused by the finite width of the crystal increases even with $(cot\Theta_B)^2$. Therefore an experiment should be performed at about $\theta_B > 40^0$. A reasonable range for the Bragg angles is $40^0 < \theta_B < 65^0$ because the detector must be well shielded from the pion source which excludes higher Bragg angles. In order to shield the CCD detector an extended concrete shielding must be tailored around the path of the X–rays and especially around the CCD detector. Therefore not even this angular range is accessible without reworking the whole shielding.
Table 5 shows that there exist very close pairs of Bragg angles for pionic hydrogen and the corresponding muonic hydrogen transitions provided the $SiO_2$100 crystal is used for muons

Transition	Energy[eV]	$\Theta_B[^0]$			
		SiO_2100	$SiO_210.1$	$SiO_211.0$	$Si111$
$\mu^- p_{2\to1}$	1896	**50.22**	78.22	–	–
$\mu^- p_{3\to1}$	2248	**40.40**	55.7	–	61.58
$\mu^- p_{4\to1}$	2371	37.88	51.52	–	56.51
$\pi^- p_{2\to1}$	2433	36.76	**49.65**	–	54.35
$\mu^- p_{\infty\to1}$	2528	35.17	47.31	87.29	51.46
$\pi^- p_{3\to1}$	2885	30.31	**40.00**	61.08	43.26
$\pi^- p_{4\to1}$	3042	28.60	37.60	56.11	40.54
$\pi^- p_{5\to1}$	3114	27.88	36.6	54.19	39.42
$\pi^- p_{\infty\to1}$	3244	26.67	34.9	51.11	37.56

Table 5: Pionic and muonic hydrogen X–rays are listed together with the Bragg angles of relevant single crystals.

and the $SiO_210.1$ crystal for pions. ***We plan to use this fact to simultaneously measure the muonic and pionic X–rays by using two suitably arranged crystals.*** In this way instabilities between a pion measurement and the reference measurement with muons cancel. The two crystals will be mounted one on top of each other symmetrically above and below a horizontal plane given by the center of the target and the CCD detector. Further implications of this approach are discussed in chapter 4.

5.4 CCD detectors.

The spatial resolution of CCD detectors together with their good energy resolution, efficiency and background rejection quality make them especially suitable for measurements with a crystal spectrometer. We will use a newly developed CCD detector system which is presently being set up for the measurement of the pion mass [86]. The detector comprises an array of 6 large area CCDs that were developed specifically for X-ray photon detection for the XMM EPIC X-ray astronomy mission[87]. Each CCD has an image area of 600×600 pixels of $(40\mu m)^2$. The CCDs are manufactured on high-resistivity epitaxial silicon for deep depletion and high quantum efficiency (plotted as a function of energy in Fig 7) and a resolution of $\sim$150eV at $6.4keV$. The array is arranged as two adjacent columns of three devices, with a total read out time of about two minutes. Read out is performed one column at a time, with data from the three CCDs being digitized in parallel. Alternate columns will be read out continously with minimum integration time. This will provide the maximum X-ray event/background event ratio, with the minimum integration time being determined mainly by data handling capabilities.
The pixel structure not only provides good spatial resolution, but also allows post processing of the data to perform background rejection. Most of these unwanted events come from the pions stopped at a rate about $\sim10^8/s$ in the region of the cyclotron trap only $\sim2m$ away. The solid angle of the detector with respect to the target is $\sim10^{-4}$ of 4π. Even with a well tuned shield the background event rate is still of the order of $100/s$, while the expected pionic or muonic X–ray event rate is about $(2-3)\cdot10^{-2}$/s . The unwanted background mainly comprises charged particle and gamma ray events. Since these events deposit their energy over several pixels, and the low energy X-ray events are mainly contained within a single pixel, event

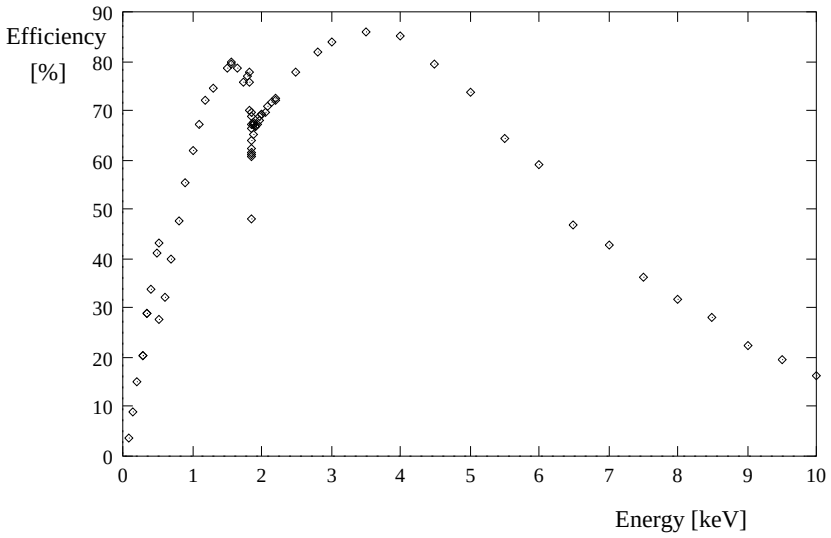

Figure 7: The intrinsic efficiency of the CCD detector is shown as a function of energy.

topology can be used to discriminate between them. Event reconstruction combined with energy discrimination can also be used to further enhance the efficiency and contribute to the high background rejection, as illustrated in Fig 6.

5.5 Shielding.

The experiment will be almost fully embedded in heavy concrete shielding. In the region between the cyclotron trap and the CCD detector more than $1m$ of concrete is needed to suppress the neutron background to a tolerable level. Between cyclotron trap and crystal box an especially tailored concrete arrangement will be designed in order to only allow a path for the X–rays.
The large mass of the shielding of about 100 tons has an additional benefit as it serves as a very efficient buffer for temperature changes as was noted in recent experiments [9].

5.6 Rate estimates.

Rate estimates are based on extensive tracking simulations and data from a feasibility study at the $\pi E5$ channel carried out with the new cyclotron trap (see Figure 6). The rates in Table 6 are given for a target gas pressure of $1bar$ and $15bar$ at room temperature on the basis of the following assumptions:

- The stop rate for pions as well as for muons is assumed to increase linearly with pressure for the pressure range considered here.
- The changes of the yields with pressure is taken into account.
- The diameter of the crystals is $90mm$. The crystals are aperture-limited to a horizontal width of $60mm$.
- The height of the CCD is $72mm$.

Transition	Int. reflectivity	Events/h	
	$[\mu rad]$	$1bar$	$15bar$
$\mu H_{2\to1}$	14.7	4	75
$\mu H_{3\to1}$	17.1	2	57
$\pi H_{2\to1}$	34.8	13	106
$\pi H_{3\to1}$	29.8	5	79
$\pi N_{6\to5}$	34.8	40	-
$\pi O_{6\to5}$	29.8	40	-

Table 6: The number of expected X–ray events/h is given for different transitions. The two pressures indicate the two typical pressure regions $1-3$ bar and $15-40$ bar. A stop rate reduction by a factor of ten is assumed for muons. The integrated reflectivity of the Si crystal used for Figure 6 was 73 μrad. The error in the quoted number of events is estimated to be on the level of 20%.

- The difference of the reflectivities of the SiO_2 crystals and the Si 111 are taken into account.

For the moment a possible improvement made by a better injection efficiency or any other kind of possible optimization is not taken into account. We take this attitude as we can not yet prove or demonstrate the exact numbers gained by improvements in future.
The pressure dependence of the rates urges to perform the experiment at higher pressures i.e. working with a cryogenic target. Therefore the experiment will start with an investigation of the $15-40$ bar region first and continue with lower pressures in a second step with a well tuned apparatus at the lowest feasible pressure. The rates of between 50 and 100 entries/h is sufficient to collect several 10^4 X–ray events in total in a three weeks measuring time. It should be recalled that about 10^4 events are sufficient to determine the shift with an accuracy of $4 \cdot 10^{-4}$ and also open the possibility to determine the width on the 10^{-2} level. The values for nitrogen and oxygen are given for a set-up optimized to pion stops. The experiment with a combination of nitrogen and oxygen gas is highly valuable as it allows for a direct check of the two–crystal method.
The numbers are also representative for other measurements like pionic Ne or C. For these gases as well as for nitrogen and oxygen the maximum tolerable partial pressure is at about $1bar$. This limitation is given by the self absorption of the low energy X–rays in the target gas.

6 Calibration of the spectrometer.

The understanding and tuning of the crystal spectrometer proceeds in different steps. These steps can be subdivided into tests without pion beam and calibrations during the experiment itself.

1. The quality of a crystal is given in terms of its intrinsic resolution and luminosity. These quantities have been measured at ESRF for the existing crystals still in flat form for different points of their surface. The reflection properties of a bent crystal spectrometer also depend on the bending process and on the chosen geometrical form

which can be influenced by shielding the $100mm$ diameter crystal disks with special diaphragms. These measurements and optimizations require a high rate of X–rays and should therefore not be performed with pion beams. We plan measurements with an ECR source which will also be used to check the two crystal setup discussed in chapter 4.3.

2. The results of step 1 must be counterchecked with pionic X–rays of negligible width. These measurements can not be done simultaneously with the pionic hydrogen measurement except perhaps the simultaneous measurement of the $\pi^- H_{3\to 1}$ with the $\pi^- O_{6\to 5}$ and the $\mu^- H_{3\to 1}$ with the $\pi^- N_{6\to 5}$, respectively. For a survey measurement with other pionic lines the spectrometer and the shielding has to be rebuilt for each measurement. Also these measurements will be partially devoted to check the two crystal set–up discussed in chapter 4.3.

3. The pionic hydrogen measurement itself will be surveyed by a simultaneous muonic hydrogen measurement with two crystals as discussed below. The validity of this method, i.e. the assumption that the relative response functions of the two crystals is sufficiently understood, must be investigated and established in step 1 and in special measurements in step 2.

6.1 Testing and tuning of the bent crystals.

A first step of a calibration and understanding the functioning of the spectrometer is a measurement with X–rays of well understood line shape in the preparatory state of the experiment. Fluorescence X–rays are not useful for this purpose as their line shape is rather complicated because of satellite structures. Also their natural width is much broader than the resolution of the available crystals. X–ray transitions of one–electron atoms are better suited as their energies are known with a precision of typically $1meV$ in the energy region of interest. The line shape is also influenced by Doppler broadening depending on the temperature which is needed to ionize the atoms in the ECR source. A Maxwellian distribution of the velocities in the ECR plasma results in a Gaussian lineshape of the X–ray lines. The temperature (energy) of the ions in the ECR plasma is not a priori known and depends on the magnetic field geometry of the ECR source as well as on the high frequency parameters. A value between $1eV$ and $10eV$ per charge value is most probable [80]. For the following estimate a value of $5eV$ per charge unit is assumed. The Doppler width is expected to be a factor of 20 higher than the natural line width for the small Z and almost a factor of 10 higher for the higher Z. This is much more favorable than the conditions with fluorescence lines. The intensity of emitted X–rays is expected to be high enough to do calibration measurements in a time much shorter (less than one hour) compared to measurements with exotic atoms which last typically some days per measured energy. It is therefore planned to set up an ECR source and do calibration measurements well before the real measurement with pions and muons [81]. These calibration measurements will start with a diagnosis of the ECR source using survey measurements with CCD detectors and then continue with a high resolution X–ray spectroscopy with Si crystals. In this way yield and Doppler width of the ECR source will be determined. In a final step the two–crystal set–up with SiO_2 crystals will be tested. In Table 7 some characteristics of one–electron lines and of fluorescence lines relevant for the required energy region are shown. At first it can be stated that no line really coincides with a muonic or pionic hydrogen transition. It can however be noted that the energies of the transitions from the one–electron

Z	M	1 e^-atoms				fluorescence lines			
		$2p_{\frac{1}{2}} \rightarrow 1s$	$\Gamma_{2p_{\frac{1}{2},\frac{3}{2}}}$	Γ_{Max}	$2p_{\frac{3}{2}} \rightarrow 1s$	$K\alpha_1$	$\Gamma_{K\alpha_2}$	$K\alpha_2$	$\Gamma_{K\alpha_2}$
		$[eV]$	$[meV]$	$[meV]$	$[eV]$	$[eV]$	$[meV]$	$[eV]$	$[meV]$
13	26.974	1727.687	11.8, 11.8	200	1729.003	1486.27	430	1486.70	430
14	27.969	2004.325	15.9, 15.8	236	2006.095	1739.38	524	1739.98	539
15	30.966	2301.651	20.9, 20.8	269	2303.982	2012.27	570	2013.7	560
16	31.963	2619.701	27.1, 26.9	311	2622.720	2306.64	769	2307.84	722
17	34.960	2958.528	34.5, 34.3	347	2962.376	2620.8	925	2622.4	945
18	39.953	3313.179	43.4, 43.1	375	3323.019	2955.63	810	2957.70	800

Table 7: Energies and line widths (FWHM) are given both for one–electron MCDF code (fully relativistic, with QED corrections and finite nuclear size) [75, 76, 77, 78] and fluorescence transitions [79] for different Z. The mass M is in nuclear mass units. The Gaussian width Γ_{Max} (FWHM) caused by a Maxwellian velocity distribution of the ECR plasma is calculated for an ion temperature of $5eV$ per charge. The widths for the fluorescence lines are from ref [73].

Z	1s2p 3P1		1s2p 1P1		1s2p 3P2		1s2s 3S1	
	energy	width	energy	width	energy	width	energy	width
	[eV]	[meV]	[eV]	[meV]	[eV]	[meV]	[eV]	[meV]
13	1588.16	0.05	1598.33	18	1588.79	1.37E-05	1575.00	1.10E-07
14	1853.80	0.10	1865.04	25	1854.69	2.55E-05	1839.47	2.37E-07
15	2140.13	0.20	2152.47	33	2141.35	4.54E-05	2124.58	4.83E-07
16	2447.19	0.38	2460.69	43	2448.78	7.77E-05	2430.40	9.39E-07
17	2775.00	0.69	2789.67	56	2777.11	1.29E-04	2756.92	1.75E-06
18	3123.58	1.18	3139.64	70	3126.34	2.07E-04	3104.18	3.15E-06
19	3493.01	1.96	3510.51	88	3496.55	3.23E-04	3472.27	5.49E-06

Table 8: Transition energies and widths for He-like transitions in the energy region covered by the crystal spectrometer.

atom of nuclear charge Z almost coincide with the fluorescence lines of Z+1 as one electron almost shields one nuclear charge. This offers the possibility to determine the peak positions of the fluorescence lines during the calibration measurement with meV precision. This more technical fact may be of help during the real measurements to check the angular precision of the spectrometer as fluorescence lines are readily available.
In Table 8 the energies and natural line widths are given for He-like atoms for transitions falling in the energy range covered by our spectrometer. The values are taken from [74] and agree well with calculations using the MCDF code [75, 76, 77, 78]. The error in the energies is on the level of some 10 meV. It can be noted that the natural line widths in some cases are very small. Also some transition pairs are suited for the test of the two-crystal arrangement.

6.2 Test experiments with pions.

As a second step we plan to determine the response function to monoenergetic lines in a special run with several pionic transitions in the energy region of interest. These lines should not be

Element	Transition	Energy[eV]
^{3}He	$3 \rightarrow 2$	1966
	$4 \rightarrow 2$	2655
	$5 \rightarrow 2$	2974
^{4}He	$3 \rightarrow 2$	1989
	$4 \rightarrow 2$	2683
	$5 \rightarrow 2$	3001
C	$5 \rightarrow 4$	2973
N	$6 \rightarrow 5$	2203
O	$6 \rightarrow 5$	2876
Ne	$7 \rightarrow 6$	2719

Table 9: Possible in situ pionic calibration lines. Only circular transitions are considered. No higher energy lines are listed as they would require higher order Bragg reflection.

influenced by strong interaction or broadening by not resolved electron screening or any kind of Doppler effect. Therefore only transitions of exotic atoms formed with monoatomic gases with $Z < 11$ can be used. Those do not exhibit Coulomb explosion during their formation and they have a high and well known degree of ionization at pressures below $100mbar$. Strong interaction broadening can be avoided for transitions high enough in the cascade. A list of appropriate transitions also including non–monoatomic gases is given in Table 9 for pionic atoms. Muonic atoms except muonic hydrogen should not be considered because of the one order of magnitude lower stop rate. It should be noted that the strong interaction $2p$ width is only of about $1meV$ for ^3He and $2meV$ for ^4He [82, 83, 84]. Molecular gases like O_2 and N_2 are included because at present the line form of these atoms is being studied intensively and will be much better known at the time of the proposal of this experiment. C is included as it will be used in the form of CH_4 for which a small Coulomb explosion [85] energy can be expected.
A dedicated run is foreseen with a special pion stop mode. In this case the pion stop rate can be further optimized as the simultaneous measurement of muonic transitions is not required. The expected rates for a mixed (N_2/O_2)target are given in chapter 3.6. The numbers for independent single gas measurements are a factor of 2 higher.

6.3 The two–crystal set–up.

Before discussing the simultaneous measurement of pionic and muonic hydrogen the question is addressed whether a simultaneous measurement of a pionic hydrogen transition together with a narrow pionic line of higher Z is feasible. In this way the determination of the response function of the detector could be carried out simultaneously to the measurement. The requirement is that the calibration lines should stem from an element which can be Bragg–reflected by one crystal onto the same detector. The energy range ΔE covered is given by the detector width Δx via the dispersion formula

$$\Delta E = \frac{E \cdot \mid \Delta x \mid}{tan(\Theta_B) \cdot sin(\Theta_B) \cdot R_c}. \tag{13}$$

For a planned width of the detector of $48mm$ the energy window has typical values between $34eV$ for the measurement of the $\mu^- H_{2\to1}$at 50.22^0 and $84eV$ for the measurement of the $\pi^- H_{3\to1}$transition at 40.00^0. For a spectroscopy of the $\mu^- H_{3\to1}$transition, however, the energy width would reduce to $22eV$ for Silicon crystal at 61.58^0. The rather narrow energy interval limits the availability of calibration lines drastically. As the stop geometry should not change during calibration the calibration line should originate from a gas admixed to hydrogen. The only line in the neighbourhood of a pionic hydrogen line is the $\pi^- O_{6\to5}$ at $2876eV$, which is only $8eV$apart from the $\pi^- H_{3\to1}$transition. This corresponds to a distance of only $4.6mm$ on the CCD if they are reflected by the 10.1 plane of SiO_2. A similar situation is given for the pair $\mu^- H_{3\to1}$ and $\pi^- N_{6\to5}$. Here the transition energies are separated by $45eV$, which corresponds to a distance of $32.8mm$ on the CCD detector for a reflection on the 100 plane of SiO_2. Unfortunately the oxygen and nitrogen lines exhibit a not well understood broadening because of an acceleration in the beginning of the cascade (Coulomb explosion) typical for molecular gases. As stated above, the understanding of these processes will improve in near future as these atoms are intensively studied with high precision [86].
It can therefore be concluded that no calibration line is available near a muonic/pionic hydrogen line if one is restricted to monoatomic gases below $Z = 10$. The $\pi^- O_{6\to5}$ and the $\pi^- N_{6\to5}$ transitions remain attractive in any case as they offer the opportunity to check the pressure independence of the hydrogen transitions energies. Therefore the target will be arranged for this special measurement that allows for a simultaneous measurement of the oxygen and nitrogen lines together with the hydrogen lines. As high statistics is not needed, a measurement time of about a week (100 hours) will be sufficient to verify the pressure independence of the energies of the muonic and pionic hydrogen $3 \to 1$ transitions.
As mentioned in chapter 3.1 and 3.3.2, two corresponding muonic and pionic hydrogen transitions can be measured simultaneously as the ratio of the lattice constants of the 100 and 10.1 planes in quartz almost coincides with the ratio of the reduced masses of muonic and pionic hydrogen. Therefore a 100 and a 10.1 quartz crystal will be mounted one on top of the other above and below the Rowland circle. Suitably arranged they can produce an image of the pionic and the muonic transition on the same detector at the same time. This offers the method to determine the response function of the apparatus with a similarly accelerated system $(\mu^- p)$ not broadened by strong interaction. As the muon mass is known with an accuracy of $3 \cdot 10^{-7}$ the muonic line also serves as a high accuracy energy standard.
The measurement with muonic hydrogen has an additional merit which is very important. Because of the small width of the transitions experimental artefacts like shifts caused by different stop distributions or absorptions in the target or target windows at different pressures can be determined. Also any cascade process or effect which up to now has escaped the attention will show up in the high resolution muonic spectra not broadened by strong interaction. To give an example, we plan to establish that the transition energy is not shifted by pressure in the density range considered. Therefore we will measure the spectra at extreme values of target pressure.
Simulated spectra of the $2 \to 1$ and the $3 \to 1$ transitions representing a measuring time of three weeks each is shown in Fig. 8 and Fig. 9, respectively.
Table 10 gives the distance of the two lines on the CCD detector together with the dispersion for the two crystals. The distance of the two foci is close enough to fit even onto one of the chips of the CCD detector. As the two crystals can still be rotated with respect to each other there is some freedom to choose the distance Δx freely.
This method can be checked as there are transition energies of electronic (to be used in the

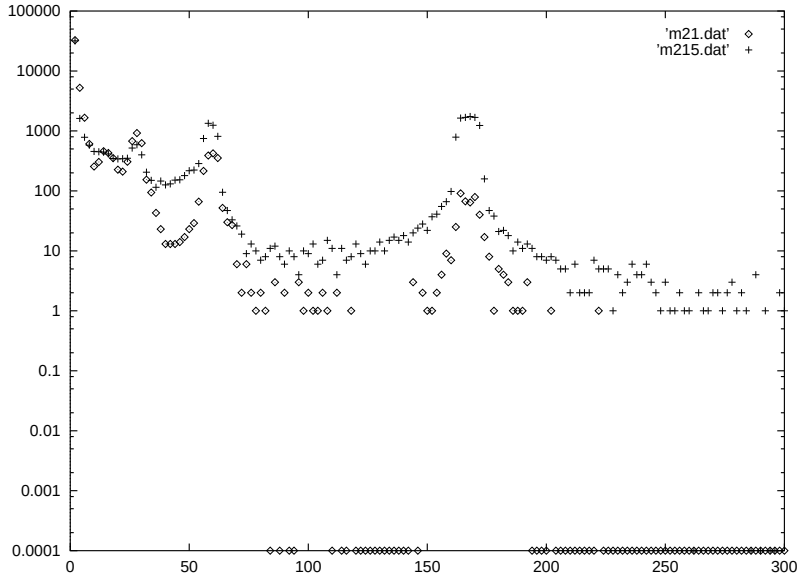

Figure 8: Simulated spectra for the $2 \rightarrow 1$ transitions in pionic (left) and muonic hydrogen as measured by a CCD detector of horizontal width of $48mm$ and a pixel size of $40\mu m$. The intensity in both lines is 40000. Both lines have a common energy resolution of $221meV$. A Lorentzian width of $950meV$ is assumed for the pionic line. The muonic line has a hyperfine splitting of $180meV$. The distribution of the kinetic energy is as in Fig. 1 and Fig. 3, respectively. The peak/background ratio for the pionic line is 100:1.

Comparison		$< \Theta_B >^0$	${\Delta_{\Theta_B}}^0$	Δx $[mm]$	D $(100)\frac{mm}{eV}$	D$(10.1)\frac{mm}{eV}$
$\mu^- H_{2\rightarrow 1}$	$\pi^- H_{2\rightarrow 1}$	49.9	.45	17.95	1.45	1.14
$\mu^- H_{3\rightarrow 1}$	$\pi^- H_{3\rightarrow 1}$	40.2	.32	10.72	0.73	0.57

Table 10: Mean Bragg angle, angle and position difference of the pionic and muonic hydrogen lines together with the dispersion of the two crystals.

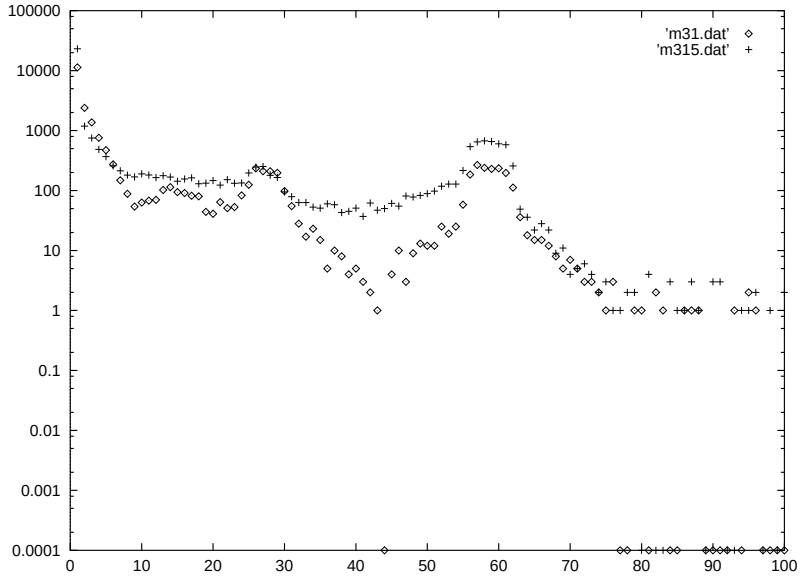

Figure 9: Simulated spectra for the $3 \rightarrow 1$ transitions in pionic (left) and muonic hydrogen as measured by a CCD detector of horizontal width of $48mm$ and a pixel size of $40\mu m$. The intensity in both lines is 40000. Both lines have a common energy resolution of $262meV$. A Lorentzian width of $950meV$ is assumed for the pionic line. The muonic line has a 1s hyperfine splitting of $180meV$. The distribution of the kinetic energy is as in Fig. 2 and Fig. 4, respectively. The peak/background ratio for the pionic line is 100:1

Comparison		$< \Theta_B >^0$	$\Delta_{\Theta_B}{}^0$	Δx $[mm]$	D $(100)\frac{mm}{eV}$	D$(10.1)\frac{mm}{eV}$
$\mu^{-4}He_{4\to2}$	$\pi^{-4}He_{4\to2}$	44.48	1.519	55	0.99	0.78
$\pi^-N_{6\to5}$	$\pi^-O_{6\to5}$	40.77	1.254	43	0.75	0.59
Si^{13+}	S^{15+}	45.80	1.624	60	1.08	0.85
P^{14+}	Cl^{16+}	39.03	0.512	17	0.66	0.52
S^{15+}	Ar^{17+}	33.85	0.135	3.9	0.43	0.34

Table 11: The angle difference and the position difference for two calibration lines is given together with the dispersion of the two crystals at the mean Bragg angle.

preparatory phase of the experiment) and exotic atoms exhibiting a similar ratio. This is the case for the ratio of line energies listed in Table 11. Fluorescence lines of corresponding pairs can also be used. For pionic and muonic ^4He and for the comparison of $Si^{13+} \leftrightarrow S^{15+}$ it is necessary to modify the geometry of the CCD detector, which does not cause a major problem. Also the comparison $S^{15+} \leftrightarrow Ar^{17+}$ is outside the nominal range of Bragg angles which is not severe during test measurements as the shielding requirements are not as stringent as in the pionic/muonic measurement. The measurement of $\pi N_{6\to5} \leftrightarrow \pi O_{6\to5}$ should be scheduled at some time during the beginning of the beam time and will consume about one week. This period is considered very important to establish the parameters for the following $\mu^-H_{3\to1} \leftrightarrow \pi^-H_{3\to1}$ and $\mu^-H_{2\to1} \leftrightarrow \pi^-H_{2\to1}$ measurements.

7 Results of simulation tests.

Spectra of Doppler broadened pionic hydrogen have been simulated and fitted for the $\pi H_{2\to1}$ and the $\pi H_{3\to1}$ transitions. The velocity profile of Figures 3 and 4 have been used for the simulation. The resolution function was taken to be gaussian with a FWHM of 221 meV and 262 meV, respectively. The Lorentzian width was assumed to be 950 meV. The peak/background ratio was assumed to be about 100:1 and the intensity in the transition was varied between 5000 and 40000 entries in the measured transition.

7.1 Independent fits.

The spectra were first fitted without using any theoretical input for the velocity distribution. The only fixed parameter was the value of the resolution function which will also be known during the real experiment. The velocity distribution was taken into account by a very crude assumption: the influence of the Doppler effect was included into the fit function by convoluting rectangular boxes corresponding to the possible Coulomb deexcitation processes. The width of the boxes was taken according to the transition energies of the allowed Coulomb deexcitations. The height of the boxes was fitted freely. This procedure resulted in the values shown in Table 12 for the relative precision in the determination of the strong interaction Lorentzian width:
It can be stated that above a certain level the increase in intensity does not any longer significantly reduce the error of the result. This feature is more pronounced for the $2 \to 1$ transition than for the $3 \to 1$ transition. Such a saturation effect in the level of precision is explained by the influence of the unknown velocity distribution which contributes to the systematic error of the fit procedure.

Transition	Intensity	relative error of Γ_L[%]
$\pi H_{3\to1}$	5000	4.9
$\pi H_{3\to1}$	10000	3.3
$\pi H_{3\to1}$	20000	2.4
$\pi H_{3\to1}$	40000	2.3
$\pi H_{2\to1}$	10000	3.4
$\pi H_{2\to1}$	20000	3.6

Table 12: Fit results as a function of intensity. A 1σ error is given.

7.2 Correlated fits.

The next step was to check how the independent fits can be improved by fitting the $\pi H_{2\to1}$ and the $\pi H_{3\to1}$ transition together by keeping the value for Γ_L identical for both spectra. This has been done for the intensity value of 10000 and 20000 entries each. As a result a reduction of the relative error from 3.3(3.4) % to 2.4% is obtained with a statistics of 10000 entries. The higher statistics of 20000 results in a reduction of the relative error from about 2.4 % to 1.9 %.
The only modest gain shows again how the accuracy of the fit results is influenced by the unknown Doppler broadening.

7.3 Constraints from the velocity distribution.

The knowledge of the velocity distribution was in a next step inserted into the fitting routine by allowing several rectangular Doppler boxes (representing monoenenergetic kinetic energies) to vary only in a limited range. It was found that a significant improvement needs at least an accuracy in the knowledge of the relative intensities of the Doppler distributions of 10%. In this case the error in the correlated fit above reduces from 2.4% to 1.7% for a statistics of 10000. The values for a statistics of 20000 decrease from 1.9% to 1.3%.

7.4 Conclusion.

It can be concluded that a proper measurement of the velocity distribution from the muonic hydrogen transitions is absolutely necessary to reach the final goal of the experiment. The muonic values together with the data on the kinetic energy distribution of the $\pi^- p$ atom at the instant of the nuclear reaction must constrain the input values for the Doppler distributions in the pionic case with a relative accuracy of better than 10% which seems feasible. This goal can be reached by using the atomic cascade model available in our group [52, 55, 62] tuned to reproduce the $\mu^- p$ X-ray data and the $\pi^- p$ nToF data. In summary the following steps are necessary for a successful experiment:

- The resolution function of the crystals have to be known with an accuracy of about 1% in the width determination. This statement holds for the knowledge of the resolution function for the single crystals and consequently for the two crystal arrangement. This knowledge is the clue to the success of the experiment and can only be reached by intensive studies of the response function of the crystals with X-ray lines of small width as provided by an ECR source.

- The width of the central peak (always regarding the hfs structure as well) in the muonic hydrogen spectra has to be measured with an accuracy of 1% in order to determine an influence of low energy (eV) components in the energy distribution of the muonic atoms.
- A first result for the width on the level of (2.5-2.0)% can be expected from correlated fits without invoking a detailed knowledge of acceleration mechanisms. This statement implies that in a survey measurement with muonic hydrogen for different pressures including liquid the required theoretical understanding of the cascade processes is established.
- A last step in the evaluation has necessarily to rely on a proper theoretical description of the exotic hydrogen cascade. The experimental knowledge gained from the muonic hydrogen spectra as well as from the neutron time of flight experiment has to be transferred to the pionic hydrogen case.

On the other hand an intensity in each of the measured spectra between 10000 and 20000 seems to be sufficient as in total 4 spectra (two transitions at two pressures) will be at the disposal of the evaluation. In this way an internal consistency check of the evaluation procedure is also possible: the result for the strong interaction width must be independent of both the transition and pressure used.

8 Proposals for scheduling.

The measurement can be subdivided into a preparatory phase with setting up and measuring with the ECR source and an on-beam phase including the measurement with pions and muons later on.

8.1 Electronic X–rays.

In order to calibrate and tune the crystal spectrometer before the measurement a source of X–rays of well known energy and sufficient intensity is needed. Presently the best realized one is an ECR source. This source consists of three main parts, a magnet providing a mirror field, a hexapole magnet and high frequency source. As mirror magnet the cyclotron trap II is ideally suited. A high frequency supply existing at PSI at the Phillips injector cyclotron (10.12 GHz, 1.5 kW) could be used as a stand by as long as no other more powerful source is available. The hexapole magnet has to be bought from industry. The technical expertise to set up and to run the ECR source exists in the institute of one of the members of the collaboration (ATOMKI Debrecen).
We propose to observe the X–rays from the ECR source in a first step directly with the CCD detector in order to determine the efficiency of the X–ray production. In this way a minimum temperature of the ECR plasma will be found for a still sufficient yield of the one–electron atoms.
In a second step a diagnosis of the line width as a function of temperature is necessary. This can be done with the available Si Bragg crystals. The response function of these crystals is well enough known for this purpose.
In a third step the crystal spectrometer with the two–crystal set–up of SiO_2 will be used.
It is planned to have 2 measurements with the ECR source of one month each in the NA hall. We assume here a number of 10^8 produced useful X-rays per second. These measurements

could take place at the end of 1998 at the very earliest but are more realistically planned for spring-summer 1999 after the measurement of the pion mass has been finished [86].

8.2 Pionic and muonic X–rays.

The first run with a hydrogen target will concentrate on the measurement of the $3 \rightarrow 1$ transition at two different pressures. We plan a total beam time of 10 weeks presumably for the year 2000. The experiment has to be set up in the $\pi E5$ area and requires the full intensity of the proton beam of 1.5 mA with the full thickness of the pion production target E.

- The running in period of 3 weeks before the hydrogen measurement should be used to perform the necessary calibration measurements with pionic atoms as mentioned in chapter 4.2. It will need a special target in order to provide a maximum number of detected X–rays.
- 1 week should be devoted to verify the pressure independence of the pionic and muonic $3 \rightarrow 1$ transition energies as mentioned in chapter 4.3. Also in this case a special target different from the one mentioned above is required in order to allow a simultaneous measurement on hydrogen and oxygen/nitrogen gas at cryogenic temperatures.
- 6 weeks are planned to measure the strong interaction width at two pressures between $15bar$ and $40bar$.

The second run period should be devoted to the $2 \rightarrow 1$ transition. A total beam time of two months is planned for the year 2001 with a preparatory phase of two weeks and two periodes of three weeks for two pressures between $15bar$ and $40bar$.
A third run of two months is planned for the year 2002 for a measurement at lower pressures. Depending on the date of the scheduling and termination of the X-ray measurement with the ECR source the pion/muon measurements are planned to start in the years 1999/2000 and will last for about three years.

Items	Jülich	Ioa.	ThCasc	PSI	Vienna	Leic.	Ne/EISI	Paris
No. of people	2	1	5	3	7	1	3	2
Theoretical support		0.5	2	0.2				0.3
beam				0.5				
presence at runs	0.4	0.2		0.6	1.2	0.2	0.6	0.4
infrastructure	0.2			0.1				
cyclotron trap				0.3				
target	0.1			0.1	1			
vacuum system	0.3			0.2				
crystals	0.2	0.3						0.1
CCD	0.1			0.1	0.5	0.2		
Shielding				0.1				
Software control	0.3							0.1
Data acquisition					0.5	0.2	0.2	0.1

Table 13: List of responsabilities for the measurement of pionic hydrogen. The entries below the second row are in units of man years and are valid for the years 2000-2002. As nearly all members of the collaboration have other duties as well the man years do not add up to the number of people. ThCasc stands for a group consisting of physicists from the universities of Aarhus and Zürich as well as from PSI and ETH Zürich dealing mainly with the theoretical problems in the description of the cascade.

9 Responsabilities and financial contributions foreseen from the different collaboratoring partners.

The responsabilities of the different collaboration partners for the measurement of pionic/muonic hydrogen are listed in Table 13.
There is no entry for the data evaluation yet as it is planned to distribute the data for evaluation among the **students** of the different participating universities who are all planning to have PhD students working on this proposal.
It is also typical for our experiment that most of the effort goes into different mechanical work necessary for each of the steps of the experiment.
In Table 14 the duties of the collaboration partners concerned with the ECR measurement are listed.
The responsabilities imply a considerable financial involvement as well. The equipment existing at the institutes of the main collaboration partners from earlier measurements (mainly at PSI) which will be used for this proposal as well adds up to a value of about a million CHF. New investments amount to a number of about 400 kCHF and are roughly listed in Table 15.

10 Special requests from PSI.

The support required from PSI concerns **manpower**, **technical** and **financial** support as well as **laboratory and floor space.**

Items	Debrecen	Jülich/Ion.	Paris	PSI	Vienna
No. of people	1	2	2	2	3
Theory		0.5	0.5		
CCD		0.2			0.5
CCD DAQ					0.5
Cyclotron trap				0.3	
Hexapole	0.1				
HF	0.1			0.1	
Crystals		0.5			
Mechanics		0.2	0.3	0.3	

Table 14: List of the responsabilities for the pre–measurement with the ECR source. The entries below the second row are in units of manyears.

	price [kCHF]	Contributors
Mechanics (Flanges, Crystal holders,..)	85	Jülich, Paris, Vienna
Vacuum pieces (incl. ECR)	75	Jülich, Paris, Vienna
Software control	15	Jülich
Fluorescence targets	15	Jülich
CCD chips + electronics	60	(Leicester), Vienna
X-ray tube	17	Jülich
Crystal adaption	20	Jülich
Cryotarget (incl cooling machine)	110	Vienna

Table 15: List of main new investments from the collaborating institutes outside PSI.

10.1 Manpower.

The group at PSI would have to care about the following items in the preparatory stage and during the experiment:

- infrastructure for the ECR test.
- setting up of the cyclotron trap for the ECR measurement.
- infrastructure of the pion/muon experiment.
- properly installed beam parameters for the pion/muon measurement.
- tuning of the cyclotron trap and its maintenance.
- organization of the shielding
- gas system.

The present number of PSI people is scarcely sufficient to fulfill all these requirements in a proper way especially during the 3 run periods. Here we ask for a substantial support to pay guest scientists of the order of 4 months per year (i.e. two guest scientists for a beam period of two months) over the running time of the experiment (3-4 years) starting with the experiments with the ECR source. This will help to have the specialists from smaller contributing partners (Debrecen, Ioaninna, Leicester) available especially in the time 1-2 weeks before the measuring time starts.

10.2 Technical support

The help of a technician is needed in the preparatory stage of the experiment and also during the running time. His work is mostly devoted to the preparation especially of the ECR measurements and later on to the mechanical changes around and inside the cyclotron trap as the optimization of the form iron and the fabrication and testing of high pressure targets and the gas supply system. In addition changes of the mechanics of the CCD detector are also a part of the duties of the PSI technician. This request represents a smooth continuation of the present situation. During the setting up of the experiment at the pion channel the different collaboration partners will put additional technical help at the disposal of the experiment.
Also the support of the magnet group at PSI is asked for on the level of one person-one month for the years 1998-1999 in order to set up the strong focussing shimming by doing 3-dimensional magnet calculations.

10.3 Financial support

As mentioned above the financial contribution of the collaborating institutes concerning existing equipment amounts to a value of more than 1 million CHF and the value of newly purchased equipment is in total about 400 kCHF. The requests from PSI concern items which belong to the infrastructure provided best by the institution on the site of the experiment and are listed in Table 16. An investment has to be made for the tailoring of a proper concrete shielding with a cost of about 10 kCHF. The running cost of the cyclotron trap including mechanical adaptions and optimizations at each step as well as the supply of cryogenic liquids and special target gases amount to about 40-60 kCHF/y. The main item to be purchased as soon as possible is the **hexapole magnet** for the ECR source.

Items	kCHF
purchase of hexapole	140
special concrete shielding	10
machining of form pieces	15
flanges, mechanics ECR	30
yearly running costs	50

Table 16: Money requested from PSI. The first four items are investments before the experiment with the pion beam starts. The corresponding money must be spent in the year 1999.

10.4 Laboratory and floor space.

For the measurement with the ECR source a special arrangement is necessary. An ideally suited space is available and reserved for our experiment in the NA hall. This hall has the same radiation safety restrictions as the pion areas which is necessary as the ECR source represents a rather strong X-ray source. In contact with the coordinator of the NA hall also an electronic barack has been foreseen.
For the measurement at the $\pi E5$ channel an electronics barack should be placed as close to the experiment as possible. As in the last years, a place near the entrance of the $\pi E3$ area is sufficient for our purpose.
Laboratory space is requested for most of the work in the direct preparation of the experiment. This would be best situated in the "Montagehalle" near the stand for the cyclotron trap. In case no new room could be found we would for some time be satisfied with space in the room WMHA/B24.

11 Safety.

Safety problems occur both during the ECR (fluorescence) measurement and the measurement with pions and muons. In addition to the safety sheet an overview of safety problems is given here in order to give more insight into the expected problems.

11.1 Measurement in the NA hall.

11.1.1 ECR source and X–ray tube.

Both the ECR source and the fluorescence X–rays will be used only in a surveyed area and the measurements are under the same restrictions as measurements in the areas of the secondary beams at PSI. A special permission to work with the ECR source and an X–ray tube to produce the fluorescence X–rays will be applied for from the authorities of the HSK.

11.1.2 Dangerous gases.

The measurements with the ECR source will be performed with gases like SiH_4 or PH_3. A special equipment will be set up. This will consist out of

1. a safety cupboard as a container of the gas bottles (available);
2. probes to detect spurious gases and an interlock system (available);
3. a special oven to destroy the gases after use (available).

Some members of the group have experience with treating similarly dangerous gases like B_2H_6. The necessary precautions will be worked out with the specialists at PSI.

11.2 Pion/muon measurement.

For these experiments we use thin walled high pressure targets filled with hydrogen working for some time at cryogenic temperatures. Some of the participants of the proposed experiment are experienced with this kind of target and their safety requirements.

12 Appendix 1: Useful formulae in crystal spectroscopy.

12.1 Some basic facts.

The scattering of X–rays of wavelength λ on crystal planes with a spacing d is described by the Bragg reflection condition

$$n \cdot \lambda = 2 \cdot d \cdot sin\Theta_B \tag{14}$$

with n being the order of reflection and Θ_B is the Bragg reflection angle. Differentiation immediately leads to an expression for the local change of the wave length with the Bragg angle Θ_B:

$$\frac{d\lambda}{\lambda} = cot\Theta_B \cdot d\Theta_B \tag{15}$$

.

With $d\Theta_B$ replaced by the intrinsic resolution ω of a crystal) the resolving power $\frac{\lambda}{d\lambda}$ at the Bragg angle Θ_B is obtained. The need to stay at reasonably high Bragg angles is obvious.
The method of Bragg reflection for energy analysis is based on the extreme angular sensitivity. Values of several $10^{-4} rad$ for ω are typical for the crystals used in the present experiment. With flat crystals, however, in general only a small part of the crystal surface fulfills the Bragg condition. In the case of the present experiment with a typical distance of $2000mm$ between X–ray source and Bragg crystal only a stripe with a width of a little less than a mm would be usable for one wavelength. In order to reach a higher rate of the X–rays the crystals are bent to an appropriate curvature. For the moment we consider only horizontal cylindrical bending of a crystal whose deflection planes are parallel to the surface ("symmetrically cut crystals"). The use of bent crystals has long be delayed as a conceptional difficulty arises because of the geometrical impossibility to satisfy simultaneously the two requirements implicit to the Bragg law. These two conditions are:

1. at all points of the surface the incidence and reflection angles must be the same as referred to the reflection planes (condition of specular reflection).

2. at all points of the surface the deflection angle of the beam must be constant in order to obey the Bragg law.

Both Bragg condition and the condition for specular reflection are illustrated in Fig 10. The condition of specular reflection requires that source and detector being on the Rowland circle and the reflecting crystal planes are bent with a radius equal to the diameter of the Rowland circle and being tangential to the Rowland circle in one point. The Bragg law requires the angle of deflection being independent of the deflection point. Both conditions meet only for symmetrical reflection at point C.
While the conditions 1. and 2. cannot be simulteneously satisfied exactly, they can be satisfied approximately at the cost of aberration. Bending the crystal with $R_c = 2 \cdot R$ (R being the Rowland radius) as proposed by H. H. Johann [70] leads to a geometrical aberration which depends on the finite width of the crystal. The broadening can still be tolerated as long as

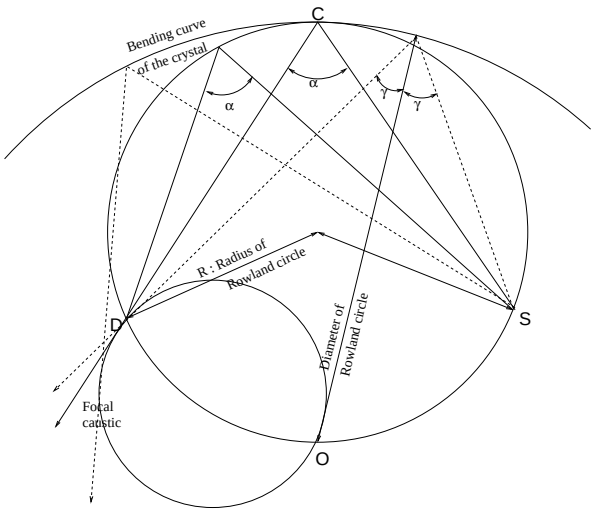

Figure 10: Rowland circle and Bragg angles. The Bragg condition requires reflection at the boundary of a circle with radius of the Rowland circle. D and S denote the position of detector and source, respectively. At C the Bragg crystal is mounted. It has a curvature radius $R_c = 2 \cdot R$ around O with R being the radius of the Rowland circle.

the contribution of the geometrical aberration is smaller than the intrinsic resolution of the crystals. This is the case for small enough crystals as used in the present experiment.
It should be mentioned that T. Johannson [88] proposed to grind the surface of a crystal bent to a radius $R_c = 2 \cdot R$ with a grinding radius R. In this way, the crystal surface is tangent to the Rowland circle and the reflecting planes still lie on a cylinder with radius $R_c = 2 \cdot R$. In the plane the Johannson geometry fulfills the focussing conditions independent of the extension of the crystal. The machining difficulties of such a procedure are tremendous.

12.1.1 Horizontal focussing.

In the following some expressions for the Johann geometry ($R_c = 2 \cdot R$) with symmetrically cut crystals are given.
The focussing condition for a Johann spectrometer yields for the distances of the source from the crystal SC or detector from the crystal DC:

$$SC = DC = R_c \cdot sin\Theta_B, \tag{16}$$

The distance from the detector (source) to the origin O of the Rowland circle are given by:

$$DO = SO = R_c \cdot cos\Theta_B. \tag{17}$$

The distance between detector and source is then given by:

$$DS = L = 2 \cdot R_c \cdot sin\Theta_B \cdot cos\Theta_B. \tag{18}$$

The detector surface is assumed to be perpendicular to the incident X–rays i.e. perpendicular to CD. The orientation in direction of DO is denoted as x with

$$dx = R_c \cdot sin\Theta_B \cdot d\Theta_B. \tag{19}$$

With the expression for the angular dispersion given above we immediately get

$$\frac{dE}{E} = cot\Theta_B \cdot dx \cdot \frac{1}{sin\Theta_B} \tag{20}$$

and from this the expression for the dispersion of the crystal:

$$\frac{dx}{dE} = \frac{R_c}{E} \cdot sin\Theta_B \cdot tan\Theta_B. \tag{21}$$

12.1.2 Vertical focussing.

Source and detector are mounted on a cylinder axis with the Bragg crystal on a cylindrical surface [89]. The crystal is bent with a curvature R_V. The distance of source to detector is given by

$$x = 2 \cdot R_V \cdot cot\Theta_B. \tag{22}$$

By invoking Bragg's law the energy dispersion is given by

$$\frac{dx}{dE} = -\frac{2\pi\hbar c}{E^2} \frac{R_V}{d \cdot cos\Theta_B \cdot sin^2\Theta_B} \tag{23}$$

or

$$\frac{dx}{dE} = -\frac{2 \cdot d \cdot R_V}{\pi \cdot \hbar \cdot c} \frac{1}{\sqrt{1 - (\frac{\pi \cdot \hbar \cdot c}{d \cdot E})^2}}. \tag{24}$$

As from the horizontal focussing condition the distance source↔detector is required to be $2R_c \cdot sin\Theta_B \cdot cos\Theta_B$ and the focal length is given by $R_c \cdot sin\Theta_B$. As these two quantities form a rectangular triangle together with R_V ($R_V^2 = R_c^2 sin^2\Theta_B - \frac{L^2}{4}$, the relation between R_V and R_C is given by

$$R_V = R_c \cdot sin^2\Theta_B. \tag{25}$$

Therefore the expression for the energy dispersion has the form

$$\frac{dx}{dE} = \frac{2\pi\hbar c}{E^2} \frac{R_c}{d \cdot cos\Theta_B} \tag{26}$$

.

In practice $R_V = 2 \cdot R = R_c$ is chosen because the otherwise necessary ellipsoidal curvature faces major technical difficulties. The loss in vertical focussing is still tolerable.

12.2 Crystal and source dimensions.

In the following the influence caused by crystal and source dimensions is discussed. We follow closely the paper by J. Eggs and K. Ulmer [90] which gives much more details. The horizontal and vertical opening angle of the crystal as seen from point O is denoted by $2 \cdot \sigma$ and $2 \cdot \varepsilon$, respectively. The height of the source is given by the opening angle $\zeta = \frac{z}{R_c}$ with z being the geometrical height of the source. The change in angle $\Delta\Theta$ caused by the finite extension of source and crystal is given by

$$\Delta\Theta = \frac{\sigma^2}{2} \cdot cot\Theta_B + \frac{\zeta^2}{sin(2 \cdot \Theta_B)}. \tag{27}$$

The angular offset caused by the height of the crystal is of the order

$$\Delta\Theta_\varepsilon = -cot^3\Theta_B \cdot \frac{\varepsilon^4}{4} \tag{28}$$

and therefore negligible for all practical purposes.

12.3 Energy resolution.

For the geometry of the proposed experiment the main contributions to the relative energy resolution are:
1. Intrinsic width of the crystal (rocking curve width of a plane crystal,see 10.4) ω :

$$\frac{\Delta E}{E} = cot\Theta_B \cdot \omega \tag{29}$$

2. Finite width b of crystal, where $\sigma = \frac{b}{2 \cdot R_c}$. The maximum energy shift along the coordinate $\boldsymbol{x}$ is given by:

$$\frac{\Delta E}{E} = \frac{\sigma^2}{2} \cdot cot^2\Theta_B \tag{30}$$

3. Height of source $\zeta = \frac{z}{R}$

$$\frac{\Delta E}{E} = \frac{\zeta^2}{2 \cdot sin^2\Theta_B} \tag{31}$$

The need to avoid small Bragg angles again becomes obvious. With σ and ζ being of the order of 10^{-2} the influence of these quantities has to be optimized during preparation experiments. The influence of the finite vertical extensions, however, disappears in this order because we measure the geometrical distribution of the reflection in the detector plane (curvature correction).

12.4 Intrinsic crystal properties.

The intrinsic properties of ideal single crystals can be calculated with an accuracy of a few percent within the framework of dynamical crystal theory [91]. The basic parameters are the rocking curve width ω, the peak reflectivity P and the integrated reflectivity R_I which are given here for plane crystals. The quantity ω is the divergence of an initially parallel beam of monoenergetic radiation after reflection on the lattice planes of a plane crystal. The peak reflectivity accounts for the maximum percentage of reflection and takes into account losses owing due to incoherent processes like photo effect in the crystal material. The integrated reflectivity is a measure for the intensity of the reflected radiation. These quantities are related by

$$R_I \sim \frac{4}{3} \cdot P \cdot \omega, \tag{32}$$

where R_I and ω are given in angular units.
Important in the case of high precision experiments is the change of the index of refraction inside the crystal material. The index of refraction shift $\Delta\Theta_{ind.}$ is almost always positive, i.e. the measured Bragg angle is given by Θ_B^{vacuum} (equation 14) plus $\Delta\Theta_{ind}$. The value of $\Delta\Theta_{ind}$ is considered to be known with an accuracy of $(2-5)\%$ if the vicinity of absorption edges is avoided. As an example the correction for the $2 \rightarrow 1$ transition in pionic hydrogen amounts to 38" for the quartz crystal used in our experiment.

12.5 Rates.

The count rate n_x from a crystal spectrometer set-up in Johann geometry is estimated by the relation

$$n_x = A_x \cdot \epsilon_{det} \cdot \eta, \tag{33}$$

where A_x denotes the activity of the source, ϵ_{det} the detection efficiency for the reflected X-rays and η the efficiency of the parameters of the Bragg crystal. Characterising the cyclotron trap by a stop efficiency f_{stop} to produce exotic atoms , the activity of the source is given by

$$A_x = N_{in} \cdot f_{stop} \cdot Y_x, \tag{34}$$

with N_{in} being the number of incoming particles and Y_x being the yield of the X-ray transition under investigation. The quantity η may be expressed by

$$\eta = \left(\frac{\Delta\Omega}{4\pi}\right) \cdot \frac{\Delta S}{S} \cdot P. \tag{35}$$

$\frac{\Delta\Omega}{4\pi}$ is the fraction of solid angle of the Bragg crystal seen from the source and P is the crystal's peak reflectivity. The quantity $\frac{\Delta S}{S}$ is the fraction of the source from which X-rays are reflected owing to the Bragg condition. For sources which can be regarded as uniformly radiating disks of radius r_s the fraction is in good approximation given by

$$\frac{\Delta S}{S} = \frac{\omega \cdot R_I \cdot sin\Theta_B \cdot 2 \cdot r_s}{\pi \cdot r_s^2} = \frac{2 \cdot R_I \cdot sin\Theta_B}{\pi \cdot r_s} \cdot \omega. \tag{36}$$

It is assumed that the dimensions of the source are small compared to the Rowland circle radius R_c.

.

13 Appendix 2: Determination of the Kinetic Energy Distribution from the Doppler Broadening of the n-ToF and X-Ray Lines.

Let $w(E)$ be the normalized kinetic energy distribution of the exotic atom, then the *cumulative* energy distribution $W(E)$ is defined by the formula

$$W(E) = \int_0^E w(E')dE' \tag{37}$$

with the normalization condition having the form

$$W(E_{max}) = \int_0^{E_{max}} w(E')dE' = 1 \tag{38}$$

where E_{max} is the maximum kinetic energy.
The neutron time of flight corresponding to the reaction $(\pi^- p)_{at} \to \pi^0 + n$ at rest is $t_0 = l/v_0$ where l is the neutron flight path and $v_0 = 0.894$ cm/ns is the neutron velocity. The Doppler broadening of the neutron time-of-flight spectrum $f(\Delta t)$, where $\Delta t = (t - t_0)$ is the difference between the measured time t and t_0, is related to the kinetic energy distribution $w(E)$ by

$$f(\Delta t) = \frac{1}{2\xi} \int_{(\Delta t/\xi)^2}^{E_{max}} \frac{w(E)}{\sqrt{E}} dE \tag{39}$$

$$\xi = t_0 \frac{c}{v_0} \sqrt{\frac{2}{M}} \tag{40}$$

where c is speed of light and M is the $\pi^- p$ mass. Given the Doppler profile $f(\Delta t)$, one can determine the cumulative energy distribution $W(E)$ using the following formula which is derived straightforwardly from Eqs.(37-40):

$$W(E) = 2 \int_0^{\xi\sqrt{E}} f(\tau)d\tau - 2\xi\sqrt{E} f(\xi\sqrt{E}) \tag{41}$$

Equation (41) can be used for the determination of the kinetic energy distribution from the measured neutron ToF spectrum in a *model independent way* as illustrated in Figs. 11, 12 and 13.
The theoretical kinetic energy distribution shown in Fig 11 corresponds to the n-ToF distribution plotted in Fig. 12. Applying Eq. (41) to the Monte Carlo generated spectrum $f(\Delta t)$ with 10^5 events we obtain perfect reconstruction of the original kinetic energy distribution as shown in Fig. 13. The Doppler broadening of the X-ray lines $g(\Delta\omega)$is described by formulas similar to Eqs. (39,40):

$$g(\Delta\omega) = \frac{1}{2\xi} \int_{(\Delta\omega/\xi)^2}^{E_{max}} \frac{w(E)}{\sqrt{E}} dE \tag{42}$$

$$\xi = \frac{\omega_0}{c} \sqrt{\frac{2}{M}} \tag{43}$$

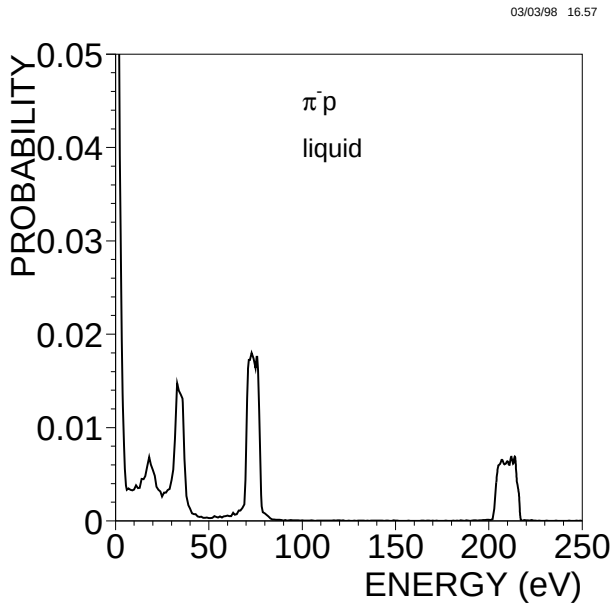

Figure 11: The calculated kinetic energy distribution of the $\pi^- p$ atom at the instant of strong interaction in liquid hydrogen.

where ω_0 is the transition energy. Therefore the same method can in principle be applied for the kinetic energy distribution of the muonic hydrogen from the Doppler profile of the X-ray lines. In this case, however, the limits of the final energy resolution are significant and proper corrections must be applied before using the formulas mentioned above. The extension to the case of pionic hydrogen, where the nuclear reaction widths should be taken into account, is straightforward.

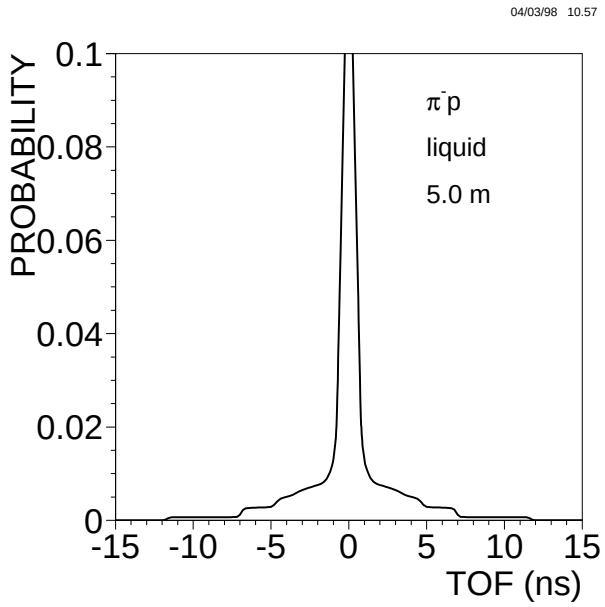

Figure 12: The calculated neutron ToF spectrum for the reaction $(\pi^- p)_{at} \to n + \pi^0$ in liquid hydrogen for a neutron flight path of 5m.

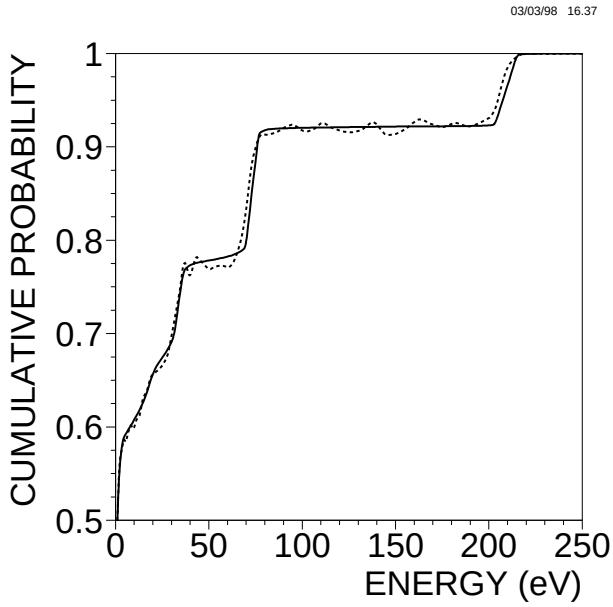

Figure 13: The cumulative energy distribution $W(E)$ reconstructed from the nToF spectrum with 10^5 events (dotted line) in comparison with the exact result corresponding to Fig 11.

List of Figures

List of Tables

References

[1] A. Forster et al., Phys. Rev. **C28** (1983) 2374.

[2] D. Bovet et al., Phys. Lett. **B153** (1985) 231.

[3] W. Beer et al., Phys. Lett. **B261** (1991) 16.

[4] D. Sigg et al., Nucl. Phys. **A 609** (1996) 269.

[5] S. Deser et al., Phys. Rev. **96** (1954) 774.

[6] G. Rasche and W.S. Woolcock, NP **A381** (1982) 405.

[7] Proposal PS212 at CERN.

[8] J. Spuller et al., Phys. Lett. **67**B (1977) 479.

[9] S. Lenz et al., Phys. Lett. **B416** (1998) 50.

[10] C. Joram et al., Phys Rev.**C 51**(1995)2144

[11] J. Gasser and H. Leutwyler, Phys. Rep. **87C** (1982) 77.

[12] E. Jenkins and A.V. Manohar, Phys. Lett. **B255** (1991) 558.

[13] J. Gasser and H. Leutwyler, Ann. Phys. (N.Y.) **158** (1984) 124.

[14] J. Gasser, H. Leutwyler, M. Locher, M. Sainio, Phys. Lett. **B213** (1988) 85.

[15] M. Locher and M. Sainio, Nucl. Phys. **A518** (1990) 201.

[16] B. Borasoy and U.-G. Meissner, Ann. Phys. (N.Y.) **254** (1997) 192.

[17] Working group on $\pi\pi$ and πN interactions, U.-G. Meißner et al., hep-ph/9711361.

[18] M.L. Goldberger, H. Miyazawa, and R. Oehme, Phys. Rev. **99** (1955) 986.

[19] H. Ch. Schröder, Diss ETH No 11760, 1996.

[20] D. Chatellard et al, Phys. Rev. Lett. **74** (1995) 4157.

[21] R. Koch, Nucl. Phys. **A448** (1986) 707.

[22] R. Koch, Z. Phys. **C29** (1985) 597.

[23] O. Dumbrajs, R. Koch, H. Pilkuhn, G.C. Oades, H. Behrens, J.J. De Swart, P. Kroll, Nucl. Phys. **B216** (1983) 277.

[24] R. Koch, E. Pietarinen, Nucl. Phys. **A336** (1980) 331.

[25] G. Höhler, in Landolt-Börnstein Numerical Data and Functional Relationships In Science and Technology, New Series, Vol.I/9B2, Ed. H. Schopper, Springer-Verlag (1983).

[26] G. Höhler, F. Kaiser, R. Koch, E. Pietarinen, Handbook of Pion Nucleon Scattering, Fachinform. Zentr., Karlsruhe (1979); Physics Data, **12-1**(1979).

[27] M.A. Kovash, πN Newsletter, **12** (1997) 51;
O. Hanstein, D. Drechsel, L. Tiator, πN Newsletter, **12** (1997) 56.

[28] R.A. Arndt, I.I. Strakovsky, R.L. Workman, M.M. Pavan, Phys. Rev. **C52** (1995) 2120.

[29] S. Weinberg, Phys. Rev. Lett. **17** (1966) 616.

[30] Y. Tomozawa, Nuovo Cim. **46A** (1966) 707.

[31] V. Bernard, N. Kaiser, U.-G. Meissner, Phys. Lett. **B309** (1993) 421.

[32] V. Bernard, N. Kaiser, U.-G. Meissner, Nucl. Phys. **B427** (1997) 483.

[33] G. Ecker and M. Mojžiš, Phys. Lett. **B365** (1996) 312.

[34] M. Mojžiš, Eur. Phys. J. **C2** (1998) 181.

[35] P.F.A. Goudsmit, H.J. Leisi, E. Matsinos, B.L. Birbrair, A.B. Gridnev, Nucl.Phys. **A575** (1994) 673.

[36] M. Locher and M. Sainio, XIII Int. Conf. on Particle and Nuclei, Perugia (1993)

[37] R.L. Workman, R.A. Arndt, M.M. Pavan, Phys. Rev. Lett. **68** (1992) 1653; **68** (1992) 2712(E).

[38] W.R. Gibbs and Li Ai, nucl-th/9704058.

[39] J. Gasser, M. Sainio, A. Svarc, Nucl. Phys. **B307** (1988) 779.

[40] V. Bernard, N. Kaiser, U.-G. Meissner, Nucl. Phys. **B388** (1992) 315.

[41] D. Sigg et al., Phys.Rev.Lett. **75** (1995) 3245.

[42] D. Sigg et al., NP A 609 (1996) 310.

[43] H. A. Bethe and E.E. Salpeter, Quantum Mechanics of
One- and Two-Electron Atoms, Academic Press Inc. NY, 1957.

[44] M. Leon and H. A. Bethe, Phys. Rev. **127** (1962)636.

[45] J.–L. Vermeulen, NP **B12** (1969)506.

[46] L. Bracci and G. Fiorentini, Nuovo Cim. **43A** (1978) 9.

[47] L. I. Men'shikov, Muon Catalyzed Fusion **2** (1988) 173.

[48] W. Czaplinski et al., Muon Catalyzed Fusion **5/6** (1990) 59.

[49] W. Czaplinski et al., Phys. Rev. **A50** (1994) 525.

[50] W. Czaplinski et al., Hyperfine Interactions **101/102** (1996) 151.

[51] V. P. Popov and V. N. Pomerantsev, Hyperfine Interactions **101,102** (1996) 133.

[52] E. C. Aschenauer and V. E. Markushin, Z. Phys. **D39** (1997) 165.

[53] L. I. Ponomarev and E. A. Solov'ev, JETP Lett. **64** (1996) 135.

[54] J. E. Crawford et al.,Phys. Rev. **D43** (1991)46.

[55] E. C. Aschenauer et al., Phys. Rev. **A51** (1995) 1965.

[56] E. C. Aschenauer and V. E. Markushin, Hyperfine Interactions **101/102** (1996) 97.

[57] A. V. Kravtsov, Contribution to the EXAT-98, 1998.

[58] V. N. Pomerantsev and V. P. Popov, Contribution to the EXAT-98, 1998.

[59] V. V. Gusev et al., Contribution to the EXAT-98, 1998.

[60] V. E. Markushin, Invited talk at EXAT-98, 1998.

[61] A. Badertscher et al., Contribution to the EXAT-98, 1998.

[62] V. E. Markushin, Phys. Rev. **A50** (1994) 1137.

[63] B. Lauss et al. Phys. Rev. Lett. **76** (1996) 4693.

[64] A. J. Rusi El Hassani et al., Z. Phys. **A351** (1995) 113.

[65] A. Badertscher et al., Phys. Lett. **B392** (1997)278.

[66] M. Daum, private communication.

[67] D. J. Abbot et al., Phys. Rev. **A55** (1997)214.

[68] D. Taqqu, F. Kottmann, private communication.

[69] D. Chatellard et al., Phys. Rev. Lett. **74** (1995) 4157.

[70] H. H. Johann, Z. Phys. **69** (1931) 185.

[71] E. Foerster, private communication

[72] G. Basile et al., Phys. Rev. Lett. **73** (1994) 3133.

[73] M. O. Krause and J. H. Oliver, J. of Physics, Chem. reference data **8** (1979) 329.

[74] W. R. Johnson, D. R. Plante, J. Sapirstein, Advances in Atomic, Molecular and Optical Physics **35** (1995) 255.

[75] P. Indelicato, O. Gorceix, and J.P. Desclaux, J. Phys. **B20** (1987)651

[76] P. Indelicato, N.I.M. **B31** (1988) 14.

[77] P. Indelicato, Phys. Rev. **A51** (1995) 1132

[78] P. Indelicato, L. de Billy, and J. P. Desclaux (unpublished)

[79] Table of Isotopes, **7.** ed., C. Michael Lederer and Virginia S. Shirley, John Wiley and Sons, Inc. (1978).

[80] P. Sortais, priv. communication.

[81] P. Sortais, Rev. Sci. Instr. **97** (1996) 867.

[82] A. Rusi el Hassani, Diss. ETH 9256, (1990)

[83] R. Landua, Dissertation, Mainz (1980)

[84] R. Landua and E. Klempt, Phys. Rev. Lett. **48** (1982)1722.

[85] J. D. Knight et al., LAMPF users Group Newsletter **11** (1979)83.

[86] PSI proposal R–97–02.1

[87] A. D. Holland et al., The MOS CCDs for the EPIC on XMM. SPIE, 2808 (1996) 414.

[88] T. Johannson, Z. Physik **82** (1933) 507.

[89] L. v. Hamos, Naturwissenschaften **20** (1932) 705.

[90] J. Eggs and K. Ulmer, Zeitschrift für angewandte Physik **20** (1965) 128.

[91] S. Brennan and P.L. Cowan, Rev. Sci. Instr. **63** (1992) 850.